nature communications

Article

https://doi.org/10.1038/s41467-024-54044-0

TET3 regulates terminal cell differentiation at the metabolic level

Received: 20 December 2023

Accepted: 29 October 2024

Isabel Mulet[1,17], Carmen Grueso-Cortina[1,17], Mireia Cortés-Cano[1,17], Daniela Gerovska[2], Guangming Wu[3,4], Stefania Alexandra Iakab[5], Daniel Jimenez-Blasco[6,7,8], Andrea Curtabbi[9], Pablo Hernansanz-Agustín[9], Harmony Ketchum[10,11,12], Israel Manjarrés-Raza[6,7,8], F. Thomas Wunderlich[13], Juan Pedro Bolaños[6,7,8], Meelad M. Dawlaty[10,11,12], Carsten Hopf[5,14], José Antonio Enríquez[8,9], Marcos J. Araúzo-Bravo[2,15,16] & Natalia Tapia[1] ✉

TET-family members play a critical role in cell fate commitment. Indeed, TET3 is essential to postnatal development due to yet unknown reasons. To define TET3 function in cell differentiation, we have profiled the intestinal epithelium at single-cell level from wild-type and *Tet3* knockout mice. We have found that *Tet3* is mostly expressed in differentiated enterocytes. In the absence of TET3, enterocytes exhibit an aberrant differentiation trajectory and do not acquire a physiological cell identity due to an impairment in oxidative phosphorylation, specifically due to an ATP synthase assembly deficiency. Moreover, spatial metabolomics analysis has revealed that *Tet3* knockout enterocytes exhibit an unphysiological metabolic profile when compared with their wild-type counterparts. In contrast, no metabolic differences have been observed between both genotypes in the stem cell compartment where *Tet3* is mainly not expressed. Collectively, our findings suggest a mechanism by which TET3 regulates mitochondrial function and, thus, terminal cell differentiation at the metabolic level.

Methylation of the cytosine base at the fifth carbon position (5-methylcytosine; 5mC) is a key epigenetic modification of DNA that regulates development and disease[1]. In mammalian cells, 5mC can be oxidized into 5-hydroxymethylcytosine (5hmC)[2]. To date, the *Ten-eleven-translocation* gene family (*Tet1*, *Tet2* and *Tet3*) are the only enzymes that have been described to convert 5mC into 5hmC through their α-ketoglutarate/Fe(II)-dependent dioxygenase activity[2].

TET enzymes seem to play an essential role in lineage specification across all three germ layers and their dysfunctions result in skewed or arrested differentiation[3–5]. Loss-of-function mouse models from the

---

[1]Stem Cell Molecular Genetics Unit, Institute of Biomedicine of Valencia, Spanish National Research Council, Valencia, Spain. [2]Group of Computational Biology and Systems Biomedicine, Biogipuzkoa Health Research Institute, San Sebastián, Spain. [3]Guangzhou National Laboratory, Guangzhou, China. [4]Department of Obstetrics and Gynecology, the Third Affiliated Hospital of Guangzhou Medical University, Guangzhou, China. [5]Center for Mass Spectrometry and Optical Spectroscopy, Manheim University of Applied Sciences, Mannheim, Germany. [6]Institute of Functional Biology and Genomics, University of Salamanca, Spanish National Research Council, Salamanca, Spain. [7]Institute of Biomedical Research of Salamanca, Salamanca, Spain. [8]Center of Biomedical Networking Research for Frailty and Healthy Ageing, Madrid, Spain. [9]Cardiovascular Regeneration Program, Centro Nacional de Investigaciones Cardiovasculares (CNIC), Madrid, Spain. [10]Ruth L. and David S. Gottesman Institute for Stem Cell and Regenerative Medicine Research, Albert Einstein College of Medicine, New York, USA. [11]Department of Genetics, Albert Einstein College of Medicine, New York, USA. [12]Department of Developmental & Molecular Biology, Albert Einstein College of Medicine, New York, USA. [13]Max Planck Institute for Metabolism Research, Cologne, Germany. [14]Medical Faculty, Heidelberg University, Heidelberg, Germany. [15]IKERBASQUE, Basque Foundation for Science, Bilbao, Spain. [16]Department of Cell Biology and Histology, Faculty of Medicine and Nursing, University of Basque Country (UPV/EHU), Leioa, Spain. [17]These authors contributed equally: Isabel Mulet, Carmen Grueso-Cortina, Mireia Cortés-Cano. ✉e-mail: ntapia@ibv.csic.es

three *Tet* family members have provided insight into their unique and overlapping functions. *Tet1* knockout mice have been described to be viable and fertile[6]. Likewise, *Tet2* knockout mice survive to an adult stage but develop lethal myeloid malignancies[7]. *Tet1* and *Tet2* double knockout mice are born at mendelian ratios but half of them die perinatally, suggesting that *Tet1* and *Tet2* enhance survival but that their loss do not impair postnatal development[8]. Remarkably, *Tet3* knockout mice develop to term but die perinatally due to unknown reasons, suggesting that *Tet1* and *Tet2* cannot compensate for *Tet3* critical functions at birth[9]. Altogether, the *Tet* paralogs exhibit functional differences that are not fully understood.

TET3 loss leads to developmental defects in multiple cell types indicating that TET3 is a crucial factor for lineage commitment and terminal differentiation[10]. In adult homeostasis, the role of *Tet3* has been studied in a few tissues together with *Tet2*, as both paralogs are expressed in many differentiated cells[5,11]. TET3 can rescue TET2 loss during hematopoietic differentiation to some lineages but not to others, suggesting that TET2 and TET3 share some but not all targets[5]. Mechanistically, TET3 has been described to be recruited, via interaction with transcription factors, to certain lineage−associated genomic loci to promote DNA demethylation and stimulate gene expression[10,12]. It has also been hypothesized that an increase in DNA hydroxymethylation levels due to TET3 activity might enhance chromatin accessibility and binding of key lineage−specific transcription factors[11]. However, the precise molecular mechanism by which TET3 physiologically regulates adult stem cell differentiation remains unresolved.

In this study, we have used the mouse intestinal epithelium as a model to investigate the role of TET3 during adult stem cell differentiation. Our data demonstrates that TET3 is required for ATP synthase assembly and, thus, is critical for mitochondrial function in cell differentiation. Overall, in the absence of TET3, enterocytes exhibit an unphysiological metabolic profile due to a deregulation in oxidative phosphorylation.

Results

Tet3 expression mainly correlates with enterocyte differentiation

To better understand the precise physiological role of TET3 in stem cell-hierarchical tissues, we generated a *Tet3* knockout mouse line through homologous recombination in which exon 5 was excised (Supp. Figure 1a). Knockout mice were born at predicted mendelian ratios but died on postnatal day (P) 1 showing no gross abnormalities (Supp. Figure 1b, c, d). 5hmC staining on whole embryo sections on embryonic day (E) 18.5 pointed to the intestinal epithelium as the tissue with the most significant reduction in 5hmC levels in the absence of TET3 (Supp. Figure 1e). Hence, we decided to focus on the intestinal epithelium for further studies assuming that the substantial decrease of 5hmC observed in this tissue might help us to pinpoint TET3 critical functions. A histological analysis of E18.5 intestinal epithelium showed no differences between the wild-type, heterozygous and *Tet3* knockout genotypes (Supp. Figure 2a). Of note, E18.5 small intestinal epithelium does not contain crypts, which develop around P5[13]. Next, we quantified RNA transcripts of the three *Tet*-family members in a cell-type specific manner with single molecule RNA fluorescent in situ hybridization (smFISH) using RNAscope probes in intestinal sections. To this end, *Tet1*, *Tet2* and *Tet3* RNAs were simultaneously detected together with *Olfm4, Vil1*, *Muc2* or *Chga* RNAs, as markers of intestinal stem cells and their progeny: enterocytes, goblet and enteroendocrine cells, respectively (Fig. 1). Paneth cells have not emerged at this developmental stage yet[14]. In each section, only the continuous intestinal epithelial monolayer containing entire villi, in which the tip and the base of each villus could be unequivocally identified, were used for subsequent cell segmentation and quantification with HALO software (Supp. Figure 2b). In the wild-type, our analysis shows that *Tet3* RNA copy number inversely correlates to *Olfm4*, *Muc2* and *Chga* RNA copy number. In contrast, a positive correlation is clearly observed between *Tet3* and *Vil1* RNA copy numbers. These results imply that *Tet3* expression increases during enterocyte maturation since *Vil1* expression is enhanced in differentiated enterocytes[15]. A spatial plot depicting the location of individual intestinal epithelial cells and their *Tet3* copy numbers is displayed in Supp. Figure 2c and reveals a pattern in which *Tet3* RNA copy numbers increase as the cells mature during their migration towards the villi tip. Likewise, a *Tet2* positive correlation with *Vil1* could also be observed (Supp. Figure 3). However, *Tet1* was only detected at very low copy numbers in very few cells and did not show a correlation to any specific cell-type marker (Supp. Figure 4). In the *Tet3* knockout intestinal epithelium, *Tet1* and *Tet2* exhibited the same expression pattern as in the wild-type (Supp. Figure 2f, 3 and 4). Quantitative RT-PCR on bulk wild-type intestinal epithelial cells demonstrated that *Tet2* and *Tet3* are expressed at similar levels (Supp. Figure 2d). The low level of *Tet1* expression identified by in situ hybridization was almost undetectable by bulk quantitative RT-PCR in both genotypes. Loss of *Tet3* expression was accompanied with an increase in *Tet2* expression levels in the *Tet3* knockout. Altogether, our findings suggest that TET2 and TET3 might play a role in enterocyte differentiation.

5hmC globally accumulates as the intestinal epithelial cells migrate upwards to the lumen (Supp. Figure 2g). Interestingly, the *Tet3* knockout intestinal epithelium exhibited a reduction in the intensity and number of 5hmC−positive cells whereas the 5hmC levels on lamina propria and interstitial space were unaffected, as shown by immunofluorescence (Supp. Figure 2g). Liquid chromatography-tandem mass spectrometry (LC-MS/MS) quantified a 50% reduction in global 5hmC levels in the *Tet3* knockout intestinal epithelium (Supp. Figure 2e). This result is in line with the intestinal epithelium being mainly composed of enterocytes and *Tet3* being mainly expressed in this cell-type (Fig. 1). *Tet2* is also expressed in enterocytes which explains the remaining 5hmC levels in the absence of TET3. Collectively, our results demonstrate that *Tet2* and *Tet3* are the *Tet*-family members responsible for 5hmC deposition in enterocytes.

TET3 is essential to acquire a physiological enterocyte signature

Next, we investigated the specific role of TET3 on enterocyte cell fate commitment. To this end, we used the single cell 10X Genomics platform to perform single-cell RNA sequencing (scRNA-seq) on 12,000 individual EpCam−positive epithelial cells sorted from the small intestine of wild-type and *Tet3* knockout E18.5 embryos (Supp. Figure 5a, b). Our analysis resolved seventeen clusters that were associated with distinct cell identities namely, stem/transit-amplifying cells (clusters 9 and 11), goblet cells (cluster 16), immature proximal and distal enterocytes (clusters 4, 6, 7, 10, 12, 14 and 15), proximal enterocytes (clusters 1, 2, 8 and 13) and distal enterocytes (clusters 0, 3 and 5), based on known markers from adult intestinal epithelium[16] since the information available for newborns is limited (Fig. 2a). The top 100 genes defining each cluster are shown in Supp. Data 1 and the 3 key genes determining the identity of each cluster are depicted in Supp Fig. 5e. Both wild-type and *Tet3* knockout goblet cells are represented by a single distinct cluster (cluster 16) that contains a similar percentage of wild-type and knockout cells (Supp. Table 1). Likewise, no major differences in gene expression and number of cells of each genotype are observed in clusters 9 and 11 that correspond to stem/transit-amplifying cells (Supp. Table 1). In contrast, enterocytes segregate in different clusters depending on their genotype, in which clusters 0, 1, 5 and 7 are mainly composed of wild-type cells whereas clusters 2, 3, 8 and 13 are composed almost entirely of *Tet3* depleted cells (Fig. 2b, c and Supp. Table 1). A trajectory analysis confirmed a bifurcating trajectory from stem/transit-amplifying cells into the secretory and the absorptive lineage and a totally different enterocyte differentiation

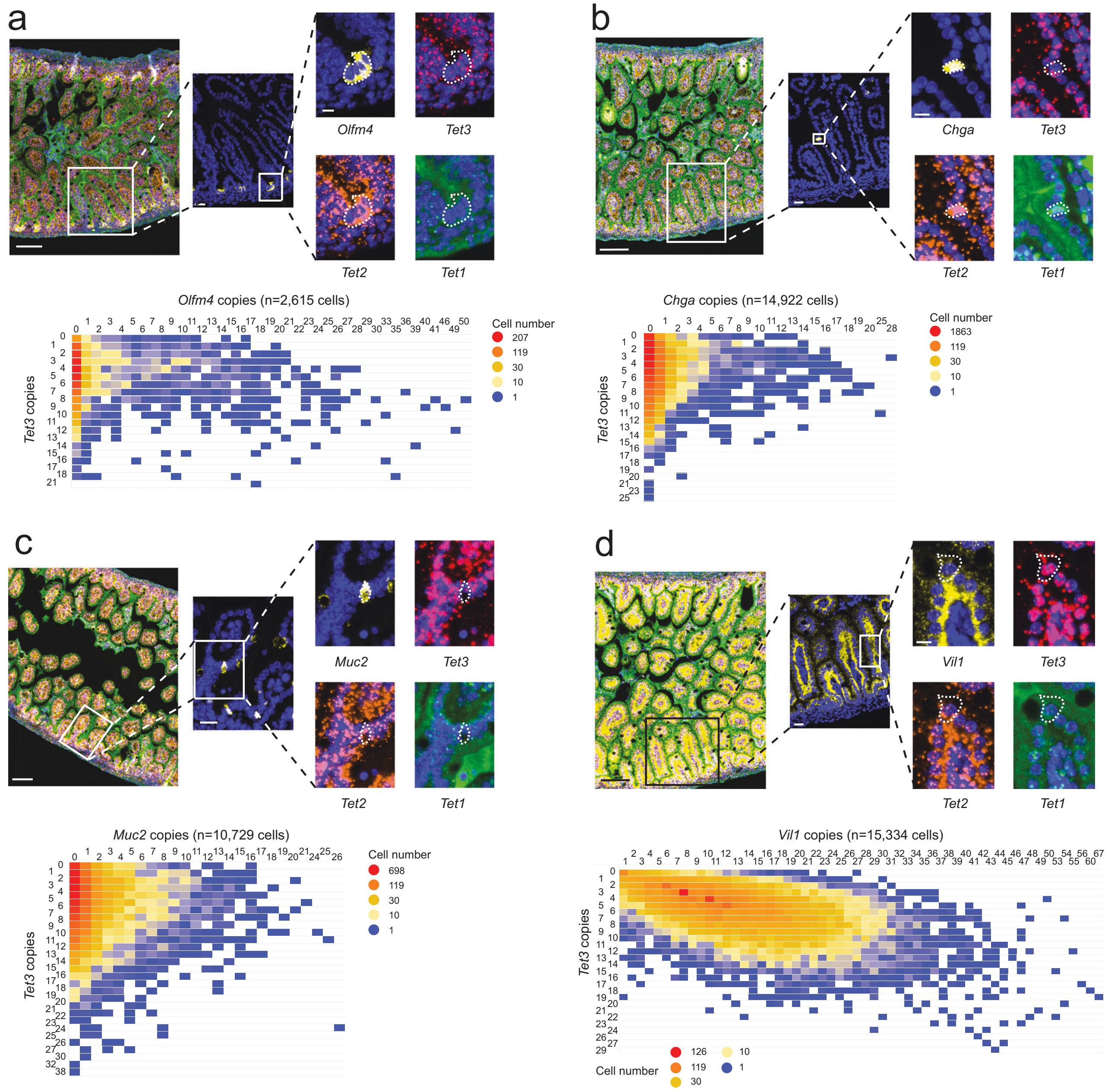

Fig. 1 | Enterocytes are the main cell-type expressing *Tet3* in the intestinal epithelium. **a**, **b**, **c** and **d** Representative images of multiplex RNAscope in situ hybridization for *Tet1*, *Tet2* and *Tet3* plus one cell type–specific marker: **a** *Olfm4* (intestinal stem cells), **b** *Chga* (enteroendocrine cells), **c** *Muc2* (goblet cells) and **d** *Vil1* (enterocytes) in wild-type intestinal epithelial sections. Scale bars represent from left to right, 100, 20 and 10 µm, respectively. **a**, **b**, **c** and **d** Co-expression of *Tet3* with each cell type–specific marker at the single-cell level in the intestinal epithelium. The axes represent the number of RNA copies detected for each gene by RNAscope in situ hybridization and the color code indicates the number of cells for each combination. The total number of analyzed cells is shown at the top. Source data are provided as a Source Data file.

trajectory between the wild-type and the *Tet3* knockout cells (Fig. 2d). Indeed, the wild-type cells progress from the stem/transit-amplifying cells into enterocytes (clusters 0, 1, 5 and 7). Instead, the majority of the *Tet3* knockout cells follow an aberrant trajectory and accumulate in clusters 2, 3, 8 and 13. These results are consistent with the positive correlation observed between *Tet3* and *Vil1* in enterocytes (Fig. 1) and indicate that most enterocytes do not reach a physiological cell identity in the absence of TET3.

A gene ontology analysis was performed to identify the main biological functions enriched only in wild-type (clusters 0, 1, 5 and 7) or only in aberrant (clusters 2, 3, 8 and 13) enterocytes. The analysis revealed a significant enrichment of oxidative phosphorylation in the wild-type (Fig. 2e, f) but of fatty acid metabolism and sterol biosynthesis in the *Tet3* knockout enterocytes (Fig. 2h, i), suggesting that energy metabolism is dysregulated in the absence of TET3. Gene set enrichment analysis between wild-type (clusters 0, 1, 5 and 7) and *Tet3* knockout (clusters 2, 3, 8 and 13) specific enterocyte clusters confirmed the oxidative phosphorylation pathway as negatively enriched in the absence of TET3 (Fig. 2g and Supp. Figure 5c, d). Indeed, a volcano plot of all the components of the mitochondrial electron transport chain showed that a large number of complex I and F_1F_0ATP synthase (also known as complex V) subunits were significantly downregulated in the *Tet3* knockout enterocytes (Fig. 2j and Supp. Figure 5f, g). Overall, our results demonstrate that the loss of TET3

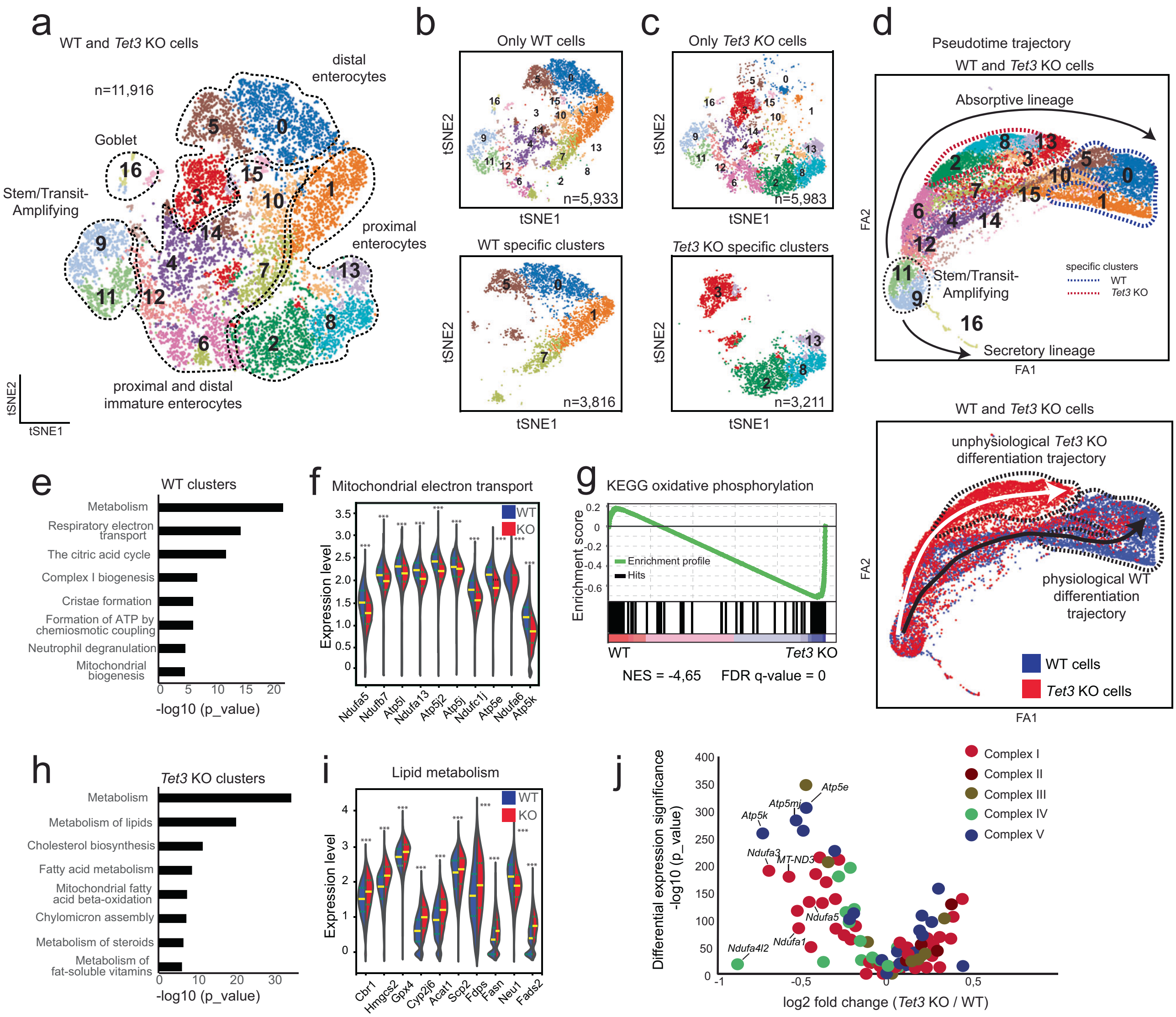

Fig. 2 | Enterocytes acquire an aberrant transcriptional signature in the absence of TET3. a Cluster color-coded scRNA-seq t-SNE visualization of 5933 E18.5 wild-type and 5983 E18.5 *Tet3* knockout small intestinal epithelial cells. Clusters are labelled with numbers and cell identities are delineated with dashed lines. **b** t-SNE visualizations of (upper panel) only wild-type cells $n = 5933$ cells and (lower panel) only wild-type specific clusters $n = 3816$ cells. **c** t-SNE visualizations of (upper panel) only *Tet3* knockout cells $n = 5983$ cells and (lower panel) only *Tet3* knockout specific clusters $n = 3211$ cells. **d** Cluster color-coded (upper panel) or genotype color-coded (lower panel) cell differentiation trajectory containing both wild-type ($n = 5933$) and *Tet3* knockout ($n = 5983$) cells for each genotype. Black and white arrows in lower panel show differentiation into the physiological and aberrant absorptive lineage, respectively. Dashed lines delimit wild-type and *Tet3* knockout–specific clusters. **e**, **h** Top 8 significantly enriched ontology terms identified using g:Profiler in specific wild-type clusters ($n = 3816$ cells) or in specific *Tet3* knockout clusters ($n = 3211$ cells), respectively. **f**, **i** Expression levels of genes representative of the mitochondrial electron transport pathway or lipid metabolism pathway in specific wild-type clusters ($n = 3816$ cells) or in specific *Tet3* knockout clusters ($n = 3211$ cells), respectively. Median as well as the first quartile and the third quartile are depicted in green and yellow, respectively. **g** GSEA plot showing oxidative phosphorylation as a negatively enriched pathway in *Tet3* knockout epithelial cells. **j** Differential expression and statistical significance between wild-type ($n = 3816$ cells) and *Tet3* knockout (n = 3211 cells) specific clusters for mitochondrial subunits showing *p*-values < 0,05. Fisher's one-tailed test with g:SCS multiple testing correction (**e, h**) and Wilcoxon rank-sum test with Benjamini-Hochberg correction (**f, i** and **j**) was used.****p*-value < 0.001. Source data are provided as a Source Data file.

leads to enterocytes with an aberrant metabolic transcriptional signature.

Mitochondrial morphology is abnormal in the absence of TET3

The gene expression analysis suggests a dysregulation in oxidative phosphorylation in the absence of TET3 (Fig. 2g). Next, we sought to ascertain the impact of TET3 loss on mitochondrial morphology as it associates with mitochondrial function[17]. In the intestinal epithelium, while the intestinal stem cells rely largely on glycolysis to fulfill their energetic demands, enterocyte dependence on oxidative phosphorylation increases with differentiation[18]. Mitochondrial elongation has been suggested to correlate with oxidative metabolism[19] and, accordingly, enterocytes exhibit more elongated mitochondria than intestinal stem cells[20]. Hence, electron microscopy analysis was employed to study the mitochondria size in the villi tip and in the intervilli region in both wild-type and *Tet3* knockout (Fig. 3a). As previously reported, the wild-type mitochondria are significantly larger in the differentiated cells located at the villus tip than at the stem cell compartment (Fig. 3b). In contrast, the mitochondrial area does not increase in the *Tet3* knockout villi tip, pointing to a mitochondrial dysfunction during intestinal epithelial cell differentiation in the absence of TET3 (Fig. 3b). Interestingly, there is no difference in

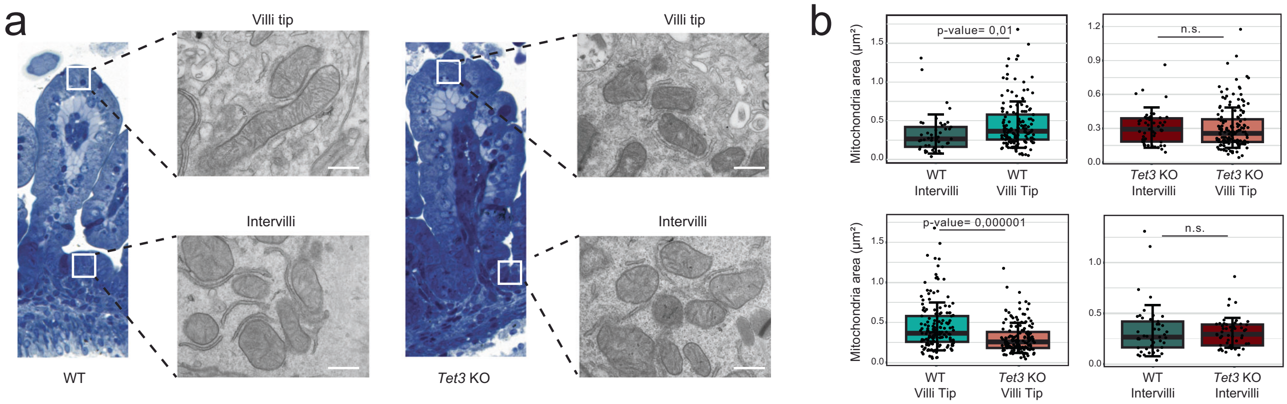

Fig. 3 | Mitochondrial morphology remains immature in the absence of TET3. **a** Representative transmission electron microscopy images from E18.5 wild-type and *Tet3* knockout mitochondria located at intervilli and villi tips are shown. Semithin sections images with boxed areas indicating the analyzed villi regions are included. Scale bars: 500 nm. **b** Quantitative mitochondrial area comparison between wild-type intervilli, *Tet3* knockout intervilli, wild-type villi tip and *Tet3* knockout villi tip ($n = 45, 53, 155$, and 150 mitochondria, respectively). Center line, median; box limits, upper and lower quartile; whiskers, 1.5x interquartile range; points, all measures. Student *t* test, two-tailed. Source data are provided as a Source Data file.

mitochondrial area between the wild-type and the *Tet3* knockout mitochondria located in the intervilli (Fig. 3b). These findings suggest that TET3 loss has no impact on the stem cell compartment and correlate with the results obtained by single cell gene expression profiling (Fig. 2d). In contrast, mitochondrial size is significantly larger in the wild-type in comparison to the *Tet3* knockout at the villi tip (Fig. 3b), indicating that mitochondria does not properly develop upon TET3 loss. Overall, mitochondria show an abnormal morphology in differentiated cells in the absence of TET3, which points to an alteration in mitochondrial fate during intestinal epithelial differentiation.

TET3 regulates mitochondrial F_1F_O-ATP synthase assembly

Tet3 knockout enterocytes showed a reduction in the expression of a large number of mitochondrial complex I and F_1F_O-ATP synthase subunits, thus we next attempt to functionally validate these results. However, isolating wild-type (clusters 0, 1, 5 and 7) and *Tet3* knockout (clusters 2, 3, 8 and 13) differentiated enterocytes is technically not feasible. Cultured fibroblasts obtained from patient skin biopsies have been previously used in the diagnostic evaluation of patients with a suspected mitochondrial disorder related to nuclear-encoded genes[21]. Therefore, we decided to assess mitochondrial complex I and ATP synthase activities in E18.5 tail tip derived-fibroblasts that, like enterocytes, also exhibit a terminally differentiated phenotype and a significant reduction in 5hmC levels (Supp. Figure 6a, b). Quantitative gene expression analysis in *Tet3* knockout fibroblasts revealed a decrease in the expression of several complex I and ATP synthase mitochondrial subunits at similar levels to those observed in *Tet3* knockout enterocytes, suggesting that the results obtained in fibroblasts could be extrapolated to enterocytes (Supp. Figure 6c). Differences in complex I assembly into supercomplexes were not observed despite the reduction in gene expression of many of its subunits, as shown by blue native gel electrophoresis (BNGE) followed by either in gel activity or western blotting for NDUFA9 (Fig. 4a). Next, we assessed the activity of mitochondrial complex I that is known to transition between active and deactive forms[22]. NADH:ubiquinone activity informs on the ability of complex I to extract electrons from NADH and transfer them to ubiquinone, allowing to determine the active form. On the other hand, NADH:$Fe(CN)_6$ oxidoreductase activity informs on the available complex I regardless if it is in active or deactive form. For the purpose of estimating both the amount of complex I and the proportion of active complex I, we measured NADH:ubiquinone and NADH:$Fe(CN)_6$ oxidoreductase activities spectrophotometrically in isolated wild-type and *Tet3* knockout mitochondria (Fig. 4b). Our results show a significant decrease in complex I NADH:$Fe(CN)_6$ but not in NADH:ubiquinone oxidoreductase activity. Altogether, our findings demonstrate that the activity of complex I is unaffected upon TET3 loss because the reduction in the total amount of complex I observed in the absence of TET3 is compensated by a higher percentage of complex I in its active form. Self-association of F_1F_O-ATP synthase monomers into rows of dimers is a fundamental biological process involved in energy efficiency[23]. In mammals, F_1F_O-ATP synthase dimerization and oligomerization is mediated by specific subunits located at the F_1F_O-ATP synthase membrane domain. Strikingly, most of the F_1F_O-ATP synthase subunits that were downregulated in both *Tet3* knockout enterocytes and fibroblasts were located in the membrane domain, as shown in the bovine F_1F_O-ATP synthase structure that is usually employed as a surrogate for mammalian homologs[24] (Fig. 4c). Hence, we used clear native gel electrophoresis to determine the oligomerization state of the ATP synthase upon TET3 loss. In gel ATPase activity and western blotting for the ATP synthase β subunit in isolated mitochondria revealed a significant decrease in the dimer/monomer ratio and a total loss of oligomers in the *Tet3* knockout fibroblasts (Fig. 4d, e). Indeed, F_1F_O-ATP synthase showed a 60% reduced activity upon TET3 loss, as measured by spectrophotometry (Fig. 4f). Next, we performed a rescue experiment in which overexpressing only the *Atp5e* subunit in *Tet3* knockout fibroblasts was almost able to recover the dimer/monomer and the oligomer/monomer ratio as well as the F_1F_O-ATP synthase activity to wild-type levels (Supp. Figures 6d, e, f). The overexpression of all the other affected subunits might be required to completely recover the phenotype. However, this rescue experiment demonstrates that a 1.5-fold reduction in *Atp5e* transcript levels is sufficient to impair ATP synthase self-assembly and activity. Mitochondrial cristae formation is inseparably linked to the formation of ATP synthase rows of dimers and a reduced dimerization ability has been described to result in widened cristae[25]. Accordingly, a larger cristae area was observed in mitochondria from *Tet3* knockout fibroblasts in comparison with their wild-type counterparts, as shown by electron microscopy (Supp. Figure 6g). In addition, we have also investigated mitochondrial morphology in heart that is considered the best tissue to detect mitochondrial functional aberrations[21]. *Tet3* knockout cardiomyocytes exhibit reduced 5hmC levels as well as smaller mitochondria, fewer developed cristae and wider cristae than their wild-type homologs (Supp. Figure 6h, k). Furthermore, we evaluated whether an ATP synthase activity reduction

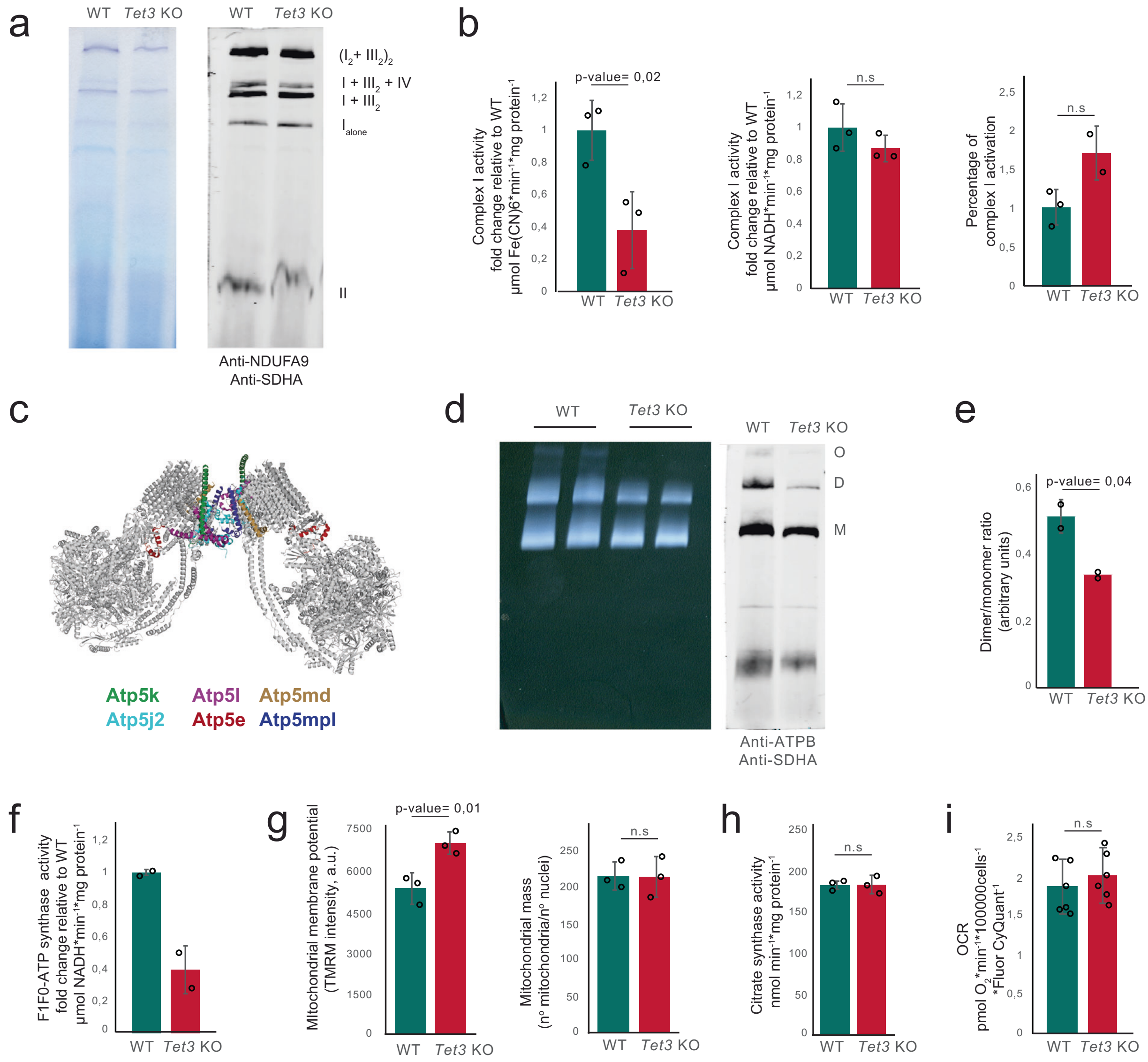

Fig. 4 | TET3 regulates mitochondrial F_1F_O-ATP synthase assembly. **a** Blue-Native gel electrophoresis followed by in gel complex I activity or western blot with anti-NDUFA9 in isolated mitochondria from wild-type and *Tet3* knockout fibroblasts. SDHA was used as loading control. I, II, III and IV refer to the different mitochondrial complexes associated into supercomplexes. Subscript number refers to the units of each complex. $n = 2$ biologically independent replicates, each sample corresponds to a pool of two independent biological samples. **b** Mitochondrial complex I NADH: Fe(CN)6 oxidoreductase (left panel) and NADH:ubiquinone (middle panel) activities spectrophotometrically measured in isolated mitochondria from wild-type and *Tet3* knockout fibroblasts. Percentage of complex I activation in isolated mitochondria (right panel). $n = 3$ biologically independent samples. **c** Bovine ATP synthase dimer state1:state3 model (PDB ID: 7AJD) in which the subunits showing lower expression levels in the absence of TET3 have been color-coded. **d** Clear native gel electrophoresis followed by in gel ATPase activity or blue native gel electrophoreses followed by western blot with anti-ATPβ from isolated mitochondria in wild-type and *Tet3* knockout fibroblasts. ATP synthase O, oligomer; D, dimer; M, monomer. $n = 2$ biologically independent replicates, each sample corresponds to a pool of two independent biological samples. **e** Dimer/monomer ratio quantification detected by in gel activity in (**d**). $n = 2$ biologically independent replicates, each sample correspond to a pool of two independent biological samples. **f** F_1F_OATP synthase activity measured spectrophotometrically in mitochondria isolated from wild-type and *Tet3* knockout fibroblasts. $n = 2$ biological replicates. **g** Mitochondrial membrane potential and mitochondrial mass quantification in wild-type and *Tet3* knockout fibroblasts, as measured by confocal imaging. $n = 3$ biologically independent samples. a.u., arbitrary units. **h** Citrate synthase activity measured spectrophotometrically in wild-type and *Tet3* knockout fibroblasts. $n = 3$ biological replicates. **i** Oxygen consumption rate (OCR)-derived quantification of basal respiration in wild-type and *Tet3* knockout fibroblasts. $n = 6$ biologically independent replicates. Data are presented as mean values +/− SD. Student's *t* test, two-tailed. Source data are provided as a Source Data file.

might contribute to mitochondrial hyperpolarization. The inner mitochondrial membrane potential was significantly increased in the absence of TET3 (Fig. 4g and Supp. Figures 6i, j), as previously described upon ATP synthase assembly impairment[26]. The mitochondrial mass, the citrate synthase activity and the cellular respiration status remained unaffected (Fig. 4g–i). Overall, our data demonstrate that TET3 loss-of-function leads to a reduction in the F_1F_O-ATP synthase self-assembly and activity.

TET3 loss-of-function leads to hypermethylation of metabolic-related pathways

TET3 can modulate gene expression through catalytic and non-catalytic activities[27,28]. To assess whether the downregulation of ATP synthase subunits upon TET3 loss was due to TET3—mediated DNA demethylation, we examined global DNA methylation patterns in wild-type and *Tet3* knockout intestinal epithelium by whole-genome bisulfite sequencing (WGBS). By mapping DNA methylation at base-pair resolution, we observed an increase in methylation levels in all analyzed genomic regions in the absence of TET3 (Fig. 5a, b).

To identify genomic regions displaying changes in 5mC levels, we searched the DNA methylome profiles for differentially methylated regions (DMRs). Consistent with TET3 catalytic role in DNA demethylation, the *Tet3* knockout epithelium showed a larger number of hypermethylated DMRs (hyperDMRs) than hypomethylated DMRs, and these hypermethylated DMRs were equally distributed across all chromosomes and gene regions (Fig. 5c, d). Ansari and collaborators have previously reported that a double *Tet2* and *Tet3* deletion in the intestinal epithelium induces profound epigenetic changes at putative enhancer regions[29]. To determine if the hyperDMRs identified in the *Tet3* knockout intestinal epithelium were enriched at enhancer regions, we used available ChIPseq data for the enhancer hallmarks H3K4me1 and H3K27ac from P0 small intestine to call enhancers[30]. We identified 16,431 enhancers and only 1497 enhancers (6,7%) overlapped with the hyperDMRs identified in the *Tet3* knockout intestinal epithelium (Fig. 5e–i). These regions were associated to 543 genes (Supp. Data 2). Our results suggest that TET3 alone does not seem to play a major role in intestinal epithelial enhancer demethylation, and that the enhancer hypermethylation observed upon combined loss of TET2 and TET3 in prior studies[29] might be largely due to *Tet2* deletion, which is known to be enriched at enhancers in many cell types. Next, all hyperDMRs as well the hyperDMRs located only at promoters were subjected to pathway enrichment analysis revealing an association with metabolism-related terms (Fig. 5j, k), as also observed at the transcriptomic level (Fig. 2e, h). Interestingly, genes encoding for ATP synthase membrane domain subunits that were downregulated upon TET3 loss were not associated to hyperDMR, excluding TET3 demethylation activity as the mechanism underlying their downregulation in gene expression.

TET3 loss-of-function impairs mitochondrial metabolic function

Our results in cultured fibroblasts demonstrating that TET3 loss-of-function leads to an ATP synthase assembly deficiency (Fig. 4) cannot be validated in the intestinal epithelium due to the inability to sort mature enterocytes. Then, we sought to assess the metabolic profile of differentiated enterocytes since an ATP synthase deficiency will certainly have an impact on cellular metabolism. To this end, an untargeted spatial metabolomic analysis was performed using matrix-assisted laser desorption/ionization mass spectrometry imaging (MALDI-MSI) to determine the relative ion intensities and spatial location of metabolites in the intestinal epithelium[31]. In total, 52 metabolites were annotated (Supp. Table 2). The base and the tip of the villi, where the proliferative and the differentiated compartments are respectively located, were separately analyzed in both the wild-type and the *Tet3* knockout intestinal epithelium (Fig. 6a). Three metabolites from the tricarboxylic acid (TCA) cycle were detected, showing non-significant differences in the intestinal stem cells but a significant increase in *Tet3* knockout differentiated enterocytes (Fig. 6b). Unfortunately, only the metabolite 3-phosphoglyceric acid could be determined from the glycolysis pathway. Again, significant higher levels were observed at the villus tip but not at the base in the absence of TET3 (Fig. 6c). The same pattern was followed by nicotinamide adenine dinucleotide (NADH) and the NAD+ precursor, nicotinamide ribotide (Fig. 6d). The redox couple glutathione (GSH) and oxidized glutathione (GSSG), which play a relevant role as non-enzymatic antioxidants, exhibited a significant increase upon TET3 loss only at the tip of the villi but not at the base (Fig. 6e). The levels of coenzyme A, that is required for fatty acid synthesis and for pyruvate oxidation in the TCA cycle, were also augmented only in the *Tet3* knockout enterocytes (Fig. 6f). Several metabolites involved in hexosamine pathway and carbohydrate biosynthesis were also higher upon TET3 loss-of-function (Fig. 6g, h). Finally, pyrimidine and purine mono- and di-nucleotides were significantly increased in the *Tet3* knockout villi tips but cytidine-, guanosine-, and uridine-5′-triphosphate showed no differences between both genotypes (Fig. 6i). Interestingly, ATP levels are significantly increased upon TET3 loss. Collectively, our results demonstrate that the *Tet3* knockout intestinal epithelium exhibits a metabolic profile that differs from its wild-type counterpart mainly at the villi tip where the differentiated enterocytes are located. Indeed, 39 metabolites were found exhibiting significant differences between the wild-type and the *Tet3* knockout only at the villi tip. On the other hand, only 3 metabolites showed significant differences only at the base between both genotypes.

Next, we analyzed the metabolic profile of tail tip–derived fibroblasts since this cell-type is used in clinical settings for the diagnosis of mitochondrial disorders[21]. Here, we could use LC-MS/MS with reference standards in order to absolutely quantify selected metabolites because spatial information is not required. We targeted our analysis on central carbon metabolism based on the molecules identified in the MALDI-MS analysis shown above. In the absence of TET3, we observed an increase in NADH as well as in NAD+ and its precursor NAAD (Supp. Figure 7a, c), a result similar to that obtained in differentiated enterocytes in which both NADH and nicotinamide ribotide were elevated upon TET3 loss. NADPH is required for fatty acid synthesis and for maintaining the steady-state level of GSH. NADPH is slightly but not significantly increased in the absence of TET3 whereas NADP+ is significantly elevated (Supp. Figure 7a). As described in Tet3 knockout enterocytes, an increment in the levels of both GSH and GSSG was observed (Supp. Figure 7a). FAD was also increased in the absence of TET3 (Supp. Figure 7b). Next, we observed a significant increment in the levels of almost all metabolites from glycolysis (Supp. Figure 7d) and a slight but significant rise in lactic acid was measured in *Tet3* knockout fibroblasts (Supp. Figure 7f). Furthermore, all the metabolites of the pentose phosphate pathway (PPP), which plays a pivotal role in the production of cellular NADPH and nucleotide biosynthesis, were elevated (Supp. Figure 7d). In fact, both pyrimidine and purine nucleotides concentrations were increased in the absence of TET3 (Supp. Figure 7e), thus correlating with the results described in *Tet3* knockout enterocytes. The metabolites involved in hexosamine pathway and tricarboxylic acid (TCA) cycle were also higher upon loss of TET3 function (Supp. Figure 7d), as in the *Tet3* knockout enterocytes. The levels of acetyl-CoA that is required for fatty acid synthesis were also augmented in the *Tet3* knockout fibroblasts (Supp. Figure 7d), in line with the elevation in coenzyme A levels detected on *Tet3* knockout enterocytes. In addition, higher levels of several glycerophospholipids, which are the major structural lipids in eukaryotic membranes[32], such as glycerophosphoetanolamine, glycerophosphoserine, glycerophosphoglycerol and glycerophosphoinositol, were also detected (Supp. Figure 7g). Moreover, acetoacetyl CoA that is essential for cholesterol synthesis also exhibited a significant increase in *Tet3*–deleted cells (Supp. Figure 7h). GDP glucose/mannose, a sugar donor for carbohydrate biosynthesis, displayed an increment in the absence of TET3 as well (Supp. Figure 7i), as in *Tet3* knockout enterocytes. Some of the enzymes involved in these metabolic pathways show substrate promiscuity and produce side products that might be toxic[33]. A significant 2-fold increase of 4-phosphoerythronate, the resulting side product generated by glyceraldehyde 3-phosphate dehydrogenase acting on erythrose-4-phosphate instead of on glyceradehyde-3-phosphate, was measured in *Tet3* knockout fibroblasts. Likewise, 2-hydroxyglutarate that arises from the noncanonical activity of several dehydrogenases also accumulates in *Tet3*-deleted fibroblasts as well as methyl-malonic acid that is a byproduct of propionate metabolism. The accumulation of these side products correlates with the observed increase in the glycolytic and TCA flux (Supp. Figure 7j). Phosphocreatine, which is considered an energy buffer[34] as well as ATP were increased in *Tet3* knockout fibroblasts (Supp. Figures. 7e, k). Nicely, ATP was also significantly increased in *Tet3* knockout enterocytes (Fig. 6i). Overall, our analysis indicates that *Tet3* knockout fibroblasts and *Tet3* knockout

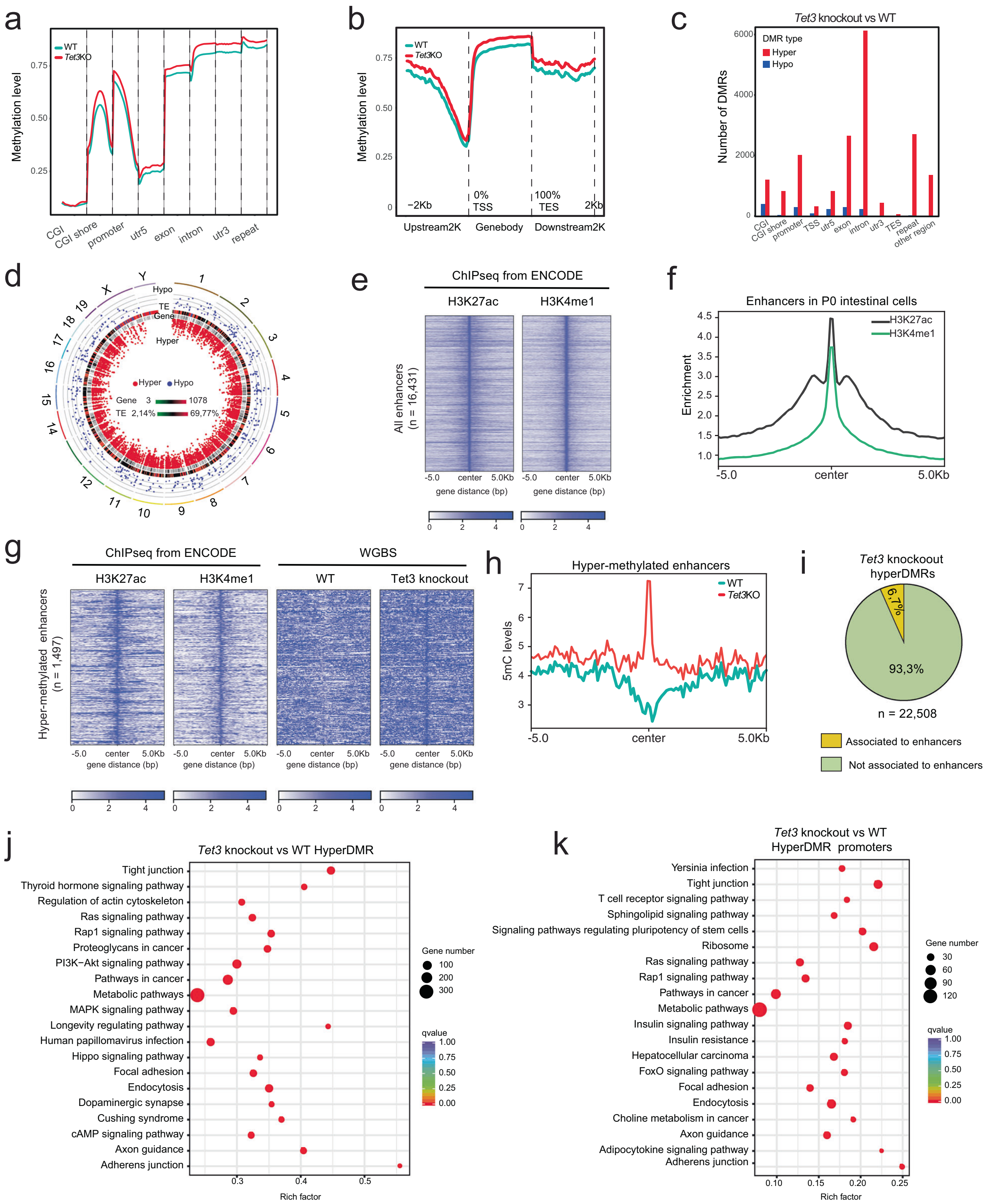

Fig. 5 | TET3 deletion leads to hypermethylation in the intestinal epithelium. a, b WGBS data represented as 5mC average levels over **a** different gene regions and **b** gene body regions for all annotated genes in wild-type and *Tet3* knockout intestinal epithelium. The methylation level has been calculated after dividing each region in 20 bins. $n = 2$ biological replicates. **c** Distribution of hyper and hypo DMRs across different gene regions. $n = 2$ biological replicates. **d** Distribution of hyper and hypo DMRs across different chromosomes. TE, repeat elements. $n = 2$ biological replicates. **e** Heatmap of H3K27ac and H3K4me1 at all enhancers identified in P0 intestinal cells. Data from ENCODE. **f** Line plot of H3K27ac and H3K4me1 enrichment at all enhancers. **g** Heatmap of H3K27ac, H3K4me1 and DNA methylation from WGBS in wild-type and *Tet3* knockout intestinal epithelium at hypermethylated enhancers. **h** DNA methylation levels at hypermethylated enhancers in *Tet3* knockout intestinal epithelial cells. **i** Percentage of hyperDMRs associated to enhancers in P0 intestinal cells. **j, k** Top 20 gene ontology terms enriched in all *Tet3* knockout hyperDMRs (**j**) or only in *Tet3* knockout hyperDMRs located at the promoter (**k**). Rich factor indicates the ratio of the number of hypermethylated genes in the pathway to the total number of genes in that pathway.

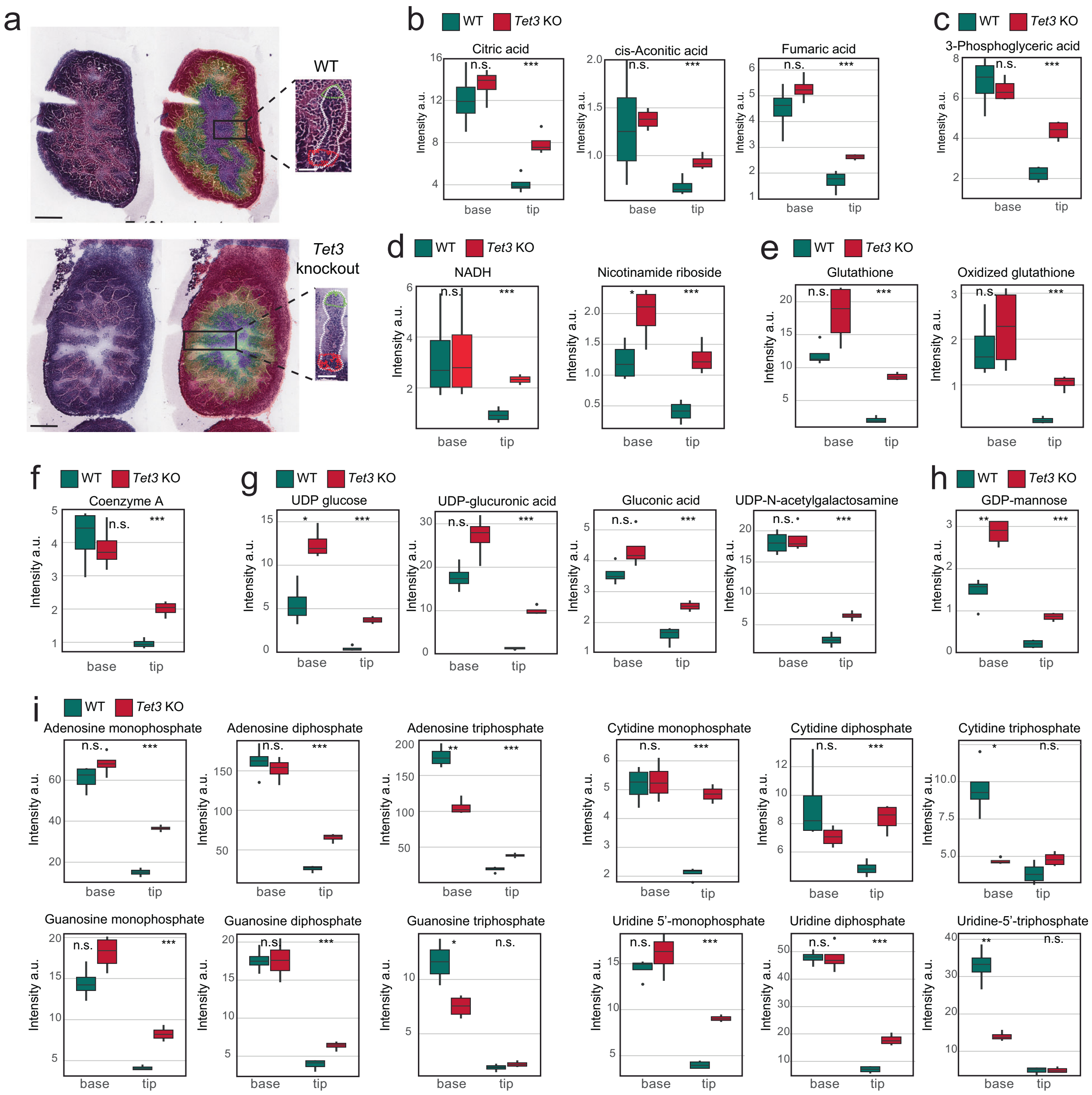

Fig. 6 | TET3 loss-of-function leads to an abnormal metabolic profile. **a** Hematoxylin and eosin–stained sections as well as MS-MALDI outlined sections for wild-type and *Tet3* knockout. Insets in the intestinal section images show the location of the magnified villus in which the measured regions are indicated. Red and green refer to base and tip, respectively. Scale bars, 200 and 50 μm **b**–**i** MALDI-MS relative quantification of metabolites. Center line refers to the median; box limits, upper and lower quartiles; whiskers 1.5x interquartile range; points, outliers. $n = 4$ independent measurements from four different histological sections. *p-value < 0,05, **p-value < 0,01 and ***p-value < 0,001. Student's t test, two-tailed. Source data are provided as a Source Data file.

enterocytes located at the villi tip show a very similar metabolic profile enriched in anabolic pathways that are reminiscent of undifferentiated cells[35]. Therefore, our study suggests that the ATP synthase deficiency observed in fibroblasts can be extrapolated to mature enterocytes since both differentiated cell types show a similar downregulation in genes coding for F_1F_0-ATP synthase membrane domain subunits, an immature mitochondrial morphology and a comparable metabolic profile. Overall, our results demonstrate that TET3 impairs mitochondrial function and compromises terminal differentiation at the metabolic level.

Discussion

In this study, we have demonstrated that enterocytes require TET3 to acquire a physiological cell identity. *Tet3* is almost not expressed at the stem cell compartment, thus both wild-type and *Tet3* knockout intestinal stem cells show an identical transcriptional profile and mitochondrial morphology. Upon differentiation, *Tet3* expression increases in the enterocytes as they migrate towards the tip of the villi. In the absence of TET3, genes coding for critical ATP synthase subunits exhibit reduced gene expression levels leading to an abnormal mitochondrial morphology and an aberrant metabolic signature specifically in enterocytes located at the tip of the villi, where *Tet3* is expressed at its highest level, but not at the base where it is almost not expressed (Fig. 3, Fig. 6 and Fig. 7). These results are in line with enterocytes–dependence on oxidative phosphorylation increasing as they mature[18]. *Tet3* knockout fibroblasts and *Tet3* knockout enterocytes exhibit a similar reduction in the expression of genes coding for ATP synthase subunits and a very similar metabolic profile. Therefore,

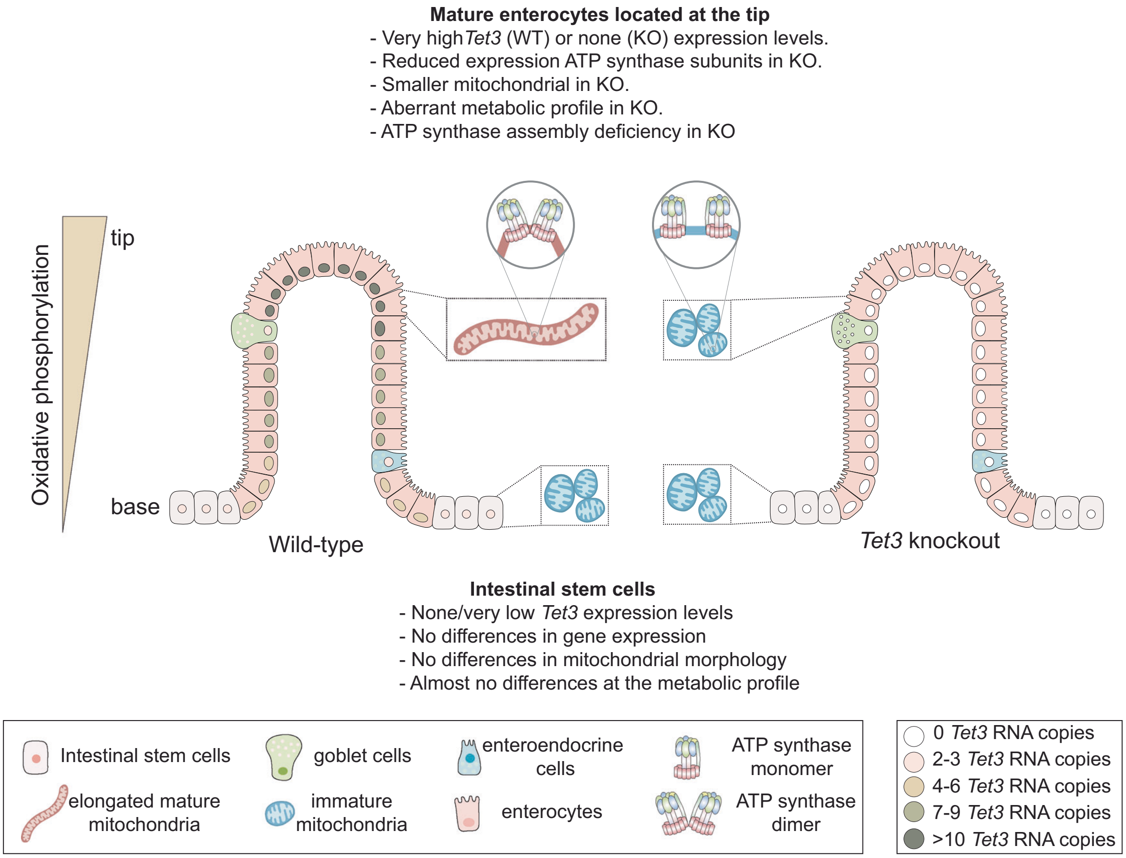

Fig. 7 | TET3 regulates terminal cell differentiation at the metabolic level. *Tet3* is almost not expressed at the stem cell compartment, thus both wild-type and *Tet3* knockout intestinal stem cells show an identical transcriptional profile and mitochondrial morphology. Upon differentiation, *Tet3* expression increases in the enterocytes as they migrate towards the tip of the villi. In the absence of TET3, genes coding for critical ATP synthase subunits exhibit reduced gene expression levels leading to an abnormal mitochondrial morphology and an aberrant metabolic signature specifically in enterocytes located at the tip of the villi, where *Tet3* is expressed at its highest level, but not at the base where it is almost not expressed (Fig. 3, Fig. 6 and Fig. 7). Finally, a biochemical analysis in fibroblasts identified an ATP synthase deficiency assembly in the absence of TET3. As *Tet3* knockout fibroblasts exhibit: i) a reduction in the expression levels of the same critical ATP synthase subunits affected in *Tet3* knockout enterocytes and; ii) a metabolic profile very similar to *Tet3* knockout enterocytes, we have extrapolated the ATP synthase impairment observed in fibroblasts to enterocytes.

we consider that the ATP synthase impairment that we have identified in *Tet3* knockout fibroblasts can be extrapolated to enterocytes (Fig. 4). A model summarizing our findings has been depicted in Fig. 7.

Two recent reports using an intestinal epithelium–specific *Tet3* or a double *Tet2* and *Tet3* conditional knockout mouse model concluded that TET3 is essential for proper epithelial differentiation but the underlying molecular mechanism was not defined[29,36]. It has also been proposed that TET3 ablation predisposes the intestinal epithelium to inflammation through microbiome alterations[29]. Likewise, another study has predicted TET enzymes to be risk genes in ulcerative colitis patients[37]. ATP synthase deficiency has been described to cause mitochondrial hyperpolarization and, in turn, an increment in the production of reactive oxygen species (ROS)[38]. Thus, our results suggest that the production of reactive species due to an ATP synthase assembly defect might be the underlying mechanism leading to the inflammation previously reported in the intestine upon TET3 loss. Furthermore, a study in the cardiac tissue showed that a cardiac-specific deletion of both *Tet2* and *Tet3* in mice leads to ventricular non-compaction cardiomyopathy with embryonic lethality[11]. Our findings might help to explain this cardiac phenotype since patients exhibiting ATP synthase deficiency due to single mutations in other ATP synthase subunits or assembling factors such as *ATP5F1D* or *TMEM70* display cardiomyopathies[39,40]. Even more, we found that *Tet3* knockout cardiomyocytes exhibit smaller mitochondria with fewer developed cristae than their wild-type homologs, supporting a mitochondrial dysfunction as the mechanism underlying the cardiomyopathy observed in the absence of *Tet2* and *Tet3*. Recently, a human Mendelian disorder caused by the disruption of *TET3* has been reported[41]. However, an insight into the disease mechanism was not described. We propose that the pathology observed in TET3 deficient patients might be due to a compromised F_1F_OATP synthase dimerization, as none of the described *TET3* mutations induce a complete TET3 loss-of-function[41], and point to *Tet3* as a new candidate gene to be considered for F_1F_O-ATP synthase deficiency diagnosis.

TET catalytic loss-of-function strongly associates to tumorigenesis since most human cancers exhibit a dramatic loss of 5hmC when compared to their normal tissue counterparts[42]. Although TET mutations can be found in some tumor types such as myeloid malignancies, gliomas and a few others, most human cancers do not contain mutations on the TET genes or their co-factors, and yet, almost every tumor analyzed to date exhibits a clear loss of 5hmC[42]. However, it is important to keep in mind that TET enzymes can be enzymatically inhibited due, for instance, to hypoxia conditions or the presence of oncometabolites. Loss-of-function mutations in TET2 are associated with diverse myeloid and lymphoid leukemia in humans, however, these mutations per se are not sufficient to induce tumorigenesis and a second unknown hit is required. *Tet2* knockout mice develop lethal myeloid malignancies at around 1-year of age[7]. Interestingly, a conditional double *Tet2* and*Tet3* knockout mouse model showed a very aggressive leukemia between 3 and 7-weeks of age but the molecular mechanism underlying this oncogenic transformation was not defined[43]. An et al. suggested that TET2-depletion leads to an impairment in double-stranded break repair mechanism[43]. Our findings demonstrate that TET3 loss establishes a metabolic program in which oxidative capacity is reduced whereas glycolysis-dependent anabolic pathways are enhanced due to mitochondria with an immature phenotype. This metabolic signature resembles the metabolic profile observed in undifferentiated cells[35] and suggests that TET3-depleted cells might be primed to malignancy transformation. Indeed, findings on TET loss in mutant mice suggest that malignant transformation occurs due to the maintenance of a stemness gene expression program[44]. Mitochondrial hyperpolarization due to compromised F_1F_O-ATP synthase dimerization and activity can generate an excess of reactive oxygen species and induce oxidative damage[26]. Hence, we hypothesize that a deficiency in double-stranded break repair mechanisms combined with an increase in oxidative stress might lead to genomic instability and oncogenic transformation in cells that, in addition, display a metabolic profile closely related to undifferentiated cells. This scenario might explain the extremely fast development of leukemias observed in the conditional double *Tet2* and*Tet3* knockout mouse model. Collectively, our analysis has revealed the molecular mechanism by which TET3 function regulates terminal differentiation at the metabolic level in enterocytes and fibroblasts. Future work will need to assess whether our findings can be extrapolated to other differentiated cell-types expressing *Tet3*.

Methods

Generation of *Tet3* knockout mice

A targeting vector introducing *loxP* sites around *Tet3* exon 5 was constructed and electroporated into (C57BL6/J x C3H/HeJ) F1 embryonic stem cells (ESCs). Deletion of the floxed region results in a frame-shift that introduces a premature stop codon in exon 6, triggering nonsense-mediated decay of the mutant transcript. The construct also contained an *FRT*-flanked selection cassette coding for neomycin and thymidine kinase. Individual neomycin-resistant ESC clones were screened for recombination in the proper genomic locus. Next, FIAU-negative selection was used to select for clones that had excised the thymidine kinase cassette after transient transfection of an Flp-coding plasmid. Then, a Cre-coding plasmid was transiently transfected to excise the *loxP*-flanked exon 5 and single ESC clones were genotyped to confirm the excision. *Tet3* knockout ESCs were used to generate chimeric mice through aggregation with morula stage (C57BL6/J x C3H/HeJ) F1 embryos. The generated male chimeric mice were crossed to CD1 females to screen for germ line transmission of the *Tet3* knockout allele. Finally, *Tet3* heterozygous females were backcrossed with pure C57BL6/JRccHsd males at least 5 generations to obtain an incipient congenic line (N5 or >95% C57BL6/JRccHsd). Genotyping primers are shown in Supp. Table 3. Mice were time-mated and the presence of a vaginal plug was considered as embryonic day (E) 0.5. Experiments were performed on E18.5 embryos obtained by caesarian section, as the gestation length of this particular mouse line is 19 days. Both male and female *Tet3* knockout mice exhibit a perinatal lethal phenotype, thus sex was not considered in the study design for not being relevant in this phenotype. Animals were housed in a controlled environment with a 12 h light/dark cycle in open cages at 20-24 °C and 55–65% humidity, with access *ad libitum* to a standard chow diet and water. All animal experiments were performed in accordance with the animal care guidelines of the European Union (2010/63/EU) prior approval of the Spanish National Research Council Ethics Committee and the Valencian Regional Government (Approval reference: 2016/VSC/PEA/00187).

RNAscope in situ hybridization and quantification analysis

The first 2 cm of E18.5 mouse small intestines that include the whole duodenum and partial jejunum from wild-type and *Tet3* knockout embryos were dissected, fixed in formalin and shipped to Charles River Laboratories Evreux. Then, the samples were embedded in paraffin, sectioned (3–5 μm thick), and stained with RNAscope probes (ACD). All images were stained with TET1 (probe 455228-C1), TET2 (probe 511598-C4), TET3 (probe 505498-C3) and one of the following cell-type specific probes: OLFM4 (311838-C2), MUC2 (315458-C2), CHGA (447858-C2) or VIL1 (463308-C2). The probe 321818 and the probe 321838 were used as positive and negative controls, respectively. The staining was performed on a Leica BOND instrument. All samples were scanned at 40x on an Akoya PhenoImager (Akoya Biosciences) and the generated qptiff files were transferred to PharmaServices team at Indica Labs for analysis. The HALO® v3.6.4 (Indica Labs) quantitative image analysis software and the HALO® FISH v3.2.3 algorithm was employed to detect and count the fluorescent RNAscope probes after cell segmentation.

Immunofluorescence, confocal microscopy and image analysis

E18.5 mouse small intestines were dissected, fixed in 4% paraformaldehyde, embedded in paraffin and sectioned (5 μm). Double stainings were performed first for 5hmC detection using the Tyramide Superboost kit (ThermoFisher Scientific) followed by stripping and second staining for 5mC. Antigen retrieval and antibody stripping was performed by incubating sections 25 min in sodium citrate buffer 10 mM pH 6 in a water bath at 95 °C. Antibodies are listed in Supp. Table 4. Images were acquired with a SP8 confocal microscope (Leica Microsystems) or a LSM980 with Airyscan2 (Zeiss) and processed using ImageJ v.1.6.0. Hematoxylin and eosin (H&E) staining was performed as previously reported[45]. Whole embryo and H&E intestine section images were obtained with an Aperio VERSA Scanner (Leica Microsystems).

5hmC quantification

DNA was extracted from epithelial cells sorted from the whole E18.5 small intestine using the Qiamp DNA Mini kit following the manufacturer's protocol. DNA was hydrolysed for 6 h at 37 °C using DNA degradase plus (Zymo Research). Mass spectrometry quantification was performed as previously described[46] in the Babraham Institute mass spectrometry facility using three individual E18.5 wild-type and three individual E18.5 *Tet3* knockout embryos.

RT - quantitative PCR

RNA was extracted from villi isolated from the whole E18.5 small intestine using the Qiamp RNeasy micro kit, including the DNAse treatment step, following the manufacturer's protocol. Quantitative PCR was performed in technical triplicates on a Quant Studio 5 Real-Time PCR System (Applied Biosystems) using Power up Sybr Green (Thermofisher) and a primer concentration of 375 nM. Primers are listed in Supp. Table 3. *Actb* and *Gapdh* were used as endogenous controls for gene expression analysis. Fold enrichment normalized to wild-type samples was calculated using the $2^{-\Delta\Delta Ct}$ method[47].

Intestine dissociation and cell sorting

A single cell suspension from whole mouse small intestinal epithelium was obtained following a previous reported protocol[48]. Briefly, the small intestine was dissected from E18.5 embryos, opened longitudinally, and placed on ice-cold PBS containing 30 mM EDTA and 1.5 mM DTT for 20 min on ice. Next, the intestine was transferred to a tube containing 30 mM EDTA in PBS, incubated at 37 °C for 10 min and, then, vigorously shaken for 30 s to release the intestinal epithelium from the lamina propria. After removing the intact intestinal muscle, the villi suspension was used for mass spectrometry quantification and whole genome bisulfite sequencing or dissociated into single cell for fluorescence activated cell sorting. To generate a single cell suspension, the villi were incubated at 37 °C for 14 min in 10 ml HBSS (with Ca^{2+} and Mg^{2+}) containing 8 mg of dispase II. During the incubation, the tube was vigorously shaken for 30 s every 2 min to dissociate the villi. Finally, 10% fetal bovine serum and 0.5 mg DNase I were added to the cellular suspension that was sequentially passed through 100 μm and 40 μm filters for obtaining single cells. The single cell suspension was incubated with CD31-PE, CD45-PE, Ter119-PE, EpCAM-APC780 fluorescent-labelled antibodies for 30 min. DAPI was used for staining dead cells. A BD FACS Aria Fusion (BD Biosciences) was used for sorting the live intestinal epithelial population (DAPI−negative, CD31-PE−negative, CD45-PE−negative, Ter119-PE−negative and EpCAM-APC780−positive cells). For all fluorescent channels, positive and negative cells were gated on the basis of fluorescent minus one control. Antibodies are listed in Supp. Table 4. For scRNA-seq, all steps were performed under RNase-free conditions and 0.5U/μl of RiboLock RNase inhibitor (ThermoFisher Scientific) was added to all buffers. Cell sorting was performed in the University of Valencia Flow Citometry Unit.

Single cell RNA-seq

Epithelial cells sorted from the whole E18.5 small intestine were fixed in 90% ice-cold methanol and stored at −80 °C until analysis. *Tet3* knockout and wild-type samples correspond to a pool of intestinal epithelial cells from two embryos each. 6000 cells per sample were analyzed. For analysis, cells were resuspended in 3x saline sodium citrate buffer containing 0.04% BSA, 1% SUPERase·In RNAs Inhibitor (Invitrogen) and 40 mM DTT[49]. Single-indexed libraries were prepared using the Chromium Single Cell 3’ v3/v3.1 chemistry (10x Genomics) following the manufacturer’s instructions. The generated libraries were sequenced on an Illumina Novaseq (Illumina) system using the following transcript read lengths: 28 bp for cell barcode and UMI, 8 bp for sample index and 91 bp for insert. 100,000 reads per cell were sequenced. scRNA-seq analysis was performed at Princess Margaret Genomics Centre (Toronto, Canada).

Single cell RNA-seq data analysis

For scRNA-seq data processing, the alevin pipeline integrated with the salmon software (version salmon-0.14.1) was used, performing cell barcode (CB) detection, read mapping, unique molecular identifier (UMI) deduplication, gene count estimation and cell barcode whitelisting[50]. Reads were aligned and annotated to the mouse GRCm38 reference genome, transcriptome and annotation, downloaded from GENOME website (version 21). Alevin’s forceCells option was set to 6000 for both wild-type and *Tet3* knockout populations to specify the number of CBs to consider for whitelisting. Standard procedures for filtering, variable gene selection, dimension reduction and clustering were performed using the Scanpy toolkit (version 1.7.1)[51]. Cells with fewer than 200 detected genes were removed from the analysis as well as cells with a mitochondrial versus all gene fraction greater than 0.15. Genes detected in more than 3 cells were considered as expressed, while genes with more than 100,000 total counts were excluded. The data matrix was total-count normalized to 10,000 reads per cell and stabilized by computing the natural logarithm of one plus the counts for each cell. Highly variable genes were filtered for feature selection, remaining a data matrix of 11871 cells (5933 WT and 5983 Tet3 knockout) and 1350 genes. Each gene was scaled to unit variance and values exceeding standard deviation 10 were clipped. For dimensional reduction and clustering, the t-Distributed Stochastic Neighbor Embedding (t-SNE)[52] and the Louvain graph-clustering method[21] were used. The ranking for the characterizing genes of each cluster was computed using the Wilcoxon test with Benjamini-Hochberg correction method. For trajectory inference, a partition-based graph abstraction (PAGA) map preserving the global topology of data was performed[51] and single-cell graphs using ‘fa’ (ForceAtlas2)[53] layout and PAGA initialization were made, one for the Louvain cluster groups, and another for the wild-type and *Tet3* knockout groups. Gene ontology analysis was performed using the *g:Profiler* web server with default parameters[54] using the top 100 gene markers for wild-type or *Tet3* knockout specific clusters. Gene Set Enrichment Analysis (GSEA) was performed with GSEA v.4.1.0 desktop software using the GSEA Preranked tool with SIGN(log2FC)*(-log10(*p*-value)) as ranking parameter for all detected genes, where SIGN is the sign operator and FC the Fold Change, and c2.cp.kegg.v7.4.symbols.gmt as enrichment gene set[55].

Transmission Electron Microscopy

Small intestines were obtained from *Tet3* knockout and wild-type 18.5 d.p.c. embryos by caesarian section. The first two centimeters of the small intestine that include the entire duodenum and jejunum were immediately fixed overnight at 4 °C by immersion in 0.1 M phosphate buffer pH 7.4, containing 4% paraformaldehyde and 2% glutaraldehyde, followed by postfixation with 1% osmium tetroxide- 0,8% potassium ferrocyanide mixture in water for 1 hour at 4 °C. Samples were then dehydrated with ethanol and propylene oxide and embedded in Epon resin. Semi-thin sections were obtained from the resin blocks and stained with toluidine blue to identify regions of interest in intestine and heart. Ultra-thin sections were stained with lead citrate and examined in a HT780 Hitachi electron microscope. Sample preparation and imaging were generated in the University of Valencia Electron Microscopy Service. Images were analyzed with ImageJ v.1.6.0.

Mitochondria isolation

Isolation of mitochondria from E18.5 tail tip−derived fibroblasts was performed from 1−3 150 mm plates, according to the differential centrifugation method. Briefly, cells were resuspended in medium A (0.32 M sucrose, 1 mM EDTA, 10 mM Tris-HCl, pH 7.4) and homogenized in a Teflon potter-type tissue homogenizer. The mixture was centrifuged at 1000 g for 5 minutes at 4 °C and the generated supernatant was subsequently centrifuged at 12,000 g for 12 minutes at 4 °C. Finally, the pellet was resuspended in medium B (25 mM sucrose, 75 mM sorbitol, 100 mM KCl, 0,05 mM EDTA, 5 mM $MgCl_2$, 10 mM Tris-HCl pH 7,4 and 10 mM H_3PO_4, final pH=7,4) and stored at −80 °C.

Mitochondria solubilization

Solubilization of mitochondrial membranes was carried out with digitonin in order to visualize both respiratory supercomplexes and free form complexes. The ratio of grams of detergent: grams of mitochondrial protein used was 4:1, except in gel where F_1F_0ATP synthase was visualized, in which the ratio was lowered to 2.5:1. 100 μg of purified mitochondria resuspended at 10 μg/μl (50 mM NaCl buffer, 50 mM imidazole and 5 mM aminocaproic acid) and containing digitonin at the desired concentration were incubated 10 minutes on ice. The insoluble portion was removed by centrifugation at 13,000 g for 30 minutes at 4 °C. The pellet obtained was discarded and the supernatant was mixed with 4x loading buffer (5% Coomassie Blue-G250 in 1 M aminocaproic acid) for gel loading.

Blue Native-PAGE and Clear Native-PAGE

3–13% gradient polyacrylamide gels were prepared in house with a gradient former. Clear native (CN) gels were essentially the same as blue native (BN) gels, but 0.01% of digitonin was added to all gel solutions and Ponceau red buffer (Ponceau red, glycerol) was used instead of the normal loading buffer. The amount of sample loaded in each well was that obtained from solubilization of 100 μg of mitochondria. Cathode buffer A (tricine 50 mM, bis-tris 15 mM, pH 7.0, Coomassie Blue G-250 0.02%) and cathode buffer B (tricine 50 mM, bis-tris 15 mM, pH 7.0, Coomassie Blue G-250 0.002%) were used for electrophoresis. Electrophoresis was performed in a cold chamber. The first half hour was run at 90 volts with cathode buffer A. After that time, the cathode buffer was exchanged for cathode buffer B. Electrophoresis continued for approximately one more hour at 300 volts, until the dye began to run out of the bottom of the gel. In CN gels the whole electrophoresis was performed in cathode buffer B, with no changes.

In-gel complex I activity

Measurement of NADH dehydrogenase activity of complex I was determined on the same gel after BN-PAGE electrophoresis. The gel was incubated in 0.1 M Tris-HCl, pH 7.4, 0.14 mM NADH and 1 mg/ml NitroBlue tetrazolium solution at room temperature. Visualization was achieved by the purple precipitate produced after reduction of NitroBlue tetrazolium by the NADH dehydrogenase activity of complex I.

In-gel F_1F_0ATP synthase activity

Measurement of NADH dehydrogenase activity of F_1F_0ATP synthase was determined on the same gel after CN-PAGE electrophoresis. The gel was incubated in 270 mM glycine, 35 mMTris, pH 8.4 for 3 hours, then ATP hydrolysis was assayed in 270 mM glycine, 35 mMTris, 4 mM ATP, 14 mMMgSO4, 0.2%Pb(NO3)2, pH 8.4. The reaction was stopped after 5–10 min by 30 min incubation in 50% methanol/50% water after the formation of phosphate lead precipitates. The gel was then scanned.

Spectrophotometric activities

Measurement of complex I activity involved a two-step measurement, as described previously[56]. First step was performed in 25 µg of 3x frozen-thawed mitochondria solubilized in Mg^{2+}-containing C1/C2 buffer, DecylCoQ 130 µM and Antimycin A 1 µM. Absorbance measurement at 37 °C, 340 nm started after addition of NADH 100 µM and lasted 2–4 min. Then, rotenone 1 µM was added and absorbance was again measured for 2–4 min. Next, 1 mM $Fe(CN)_6$ was added and measurement was performed at 420 nm at 37° for 2–4 min. Later, Diphenyleneiodonium chloride (DPI) was added and absorbance was again captured in the same conditions. F_1F_0ATP synthase activity was measured as a readout of its ATPase activity. As previously reported[57], oligomycin-sensitive ATPase activity was calculated after measuring changes in absorbance at 340 nm driven by the pyruvate kinase reaction coupled to ADP phosphorylation by F_1F_0ATP synthase.

Analysis of mitochondrial membrane potential

For mitochondrial membrane potential imaging, E18.5 tail tip—derived wild-type and *Tet3* knockout fibroblasts were seeded onto 96-well plates (PerkinElmer) and mitochondrial inhibitors were added at Krebs Ringer Phosphate Glucose buffer (KRPG) supplemented with NaCl 145 mM; Na_2HPO_4 5,7 mM; KCl 4,86 mM; $CaCl_2$ 0,54 mM; $MgSO_4$ 1,22 mM; glucose 20 mM; pH 7,35. Next, cells were loaded with 10 nM TMRM (Sigma-Aldrich) and 1 µM cyclosporine-H (Sigma-Aldrich) in the Operetta CLS microscope (30 min at 37 °C in a 5 % CO_2 atmosphere) and confocal images were acquired at 40X, 1.4 NA objective (PerkinElmer). Mitochondrial uncoupler carbonyl cyanide *p*-tri-fluoromethoxyphenylhydrazone (FCCP, 10 µM, 15 min, Sigma-Aldrich) was added as a control of mitochondrial depolarization. Finally, images were analyzed using Harmony software (PerkinElmer).

Citrate synthase activities

E18.5 tail tip—derived fibroblasts from wild-type and *Tet3* knockout embryos were snap-frozen. After three cycles of freeze/thawing, to ensure cellular disruption, citrate synthase activities were determined. Citrate synthase activity was measured in the presence of 93 mM Tris-HCl, 0.1% (vol/vol), Triton X-100, 0.2 mM acetyl-CoA and 0.2 mM DTNB; the reaction was started with 0.2 mM oxaloacetate, and the absorbance was recorded at 412 nm (30 °C) ($e = 13.6\ mM^{-1}\cdot cm^{-1}$)[58]. The protein concentration of the samples was quantified by the BCA protein assay kit (Thermofisher) following the manufacturer's instructions, using BSA as a standard.

Oxygen consumption measurement

Oxygen consumption assays were performed as previously reported[59]. Briefly, oxygen consumption rate (OCR) was measured using an XF96 Extracellular Flux Analyzer (Seahorse Bioscience). E18.5 tail tip—derived fibroblasts were plated 1 day before the experiment and pre-incubated with unbuffered DMEM 1 h at 37 °C in an incubator without CO_2 regulation. Successive injections of unbuffered DMEM, 5 µg/mL oligomycin, 300 nM carbonyl cyanide 4-(trifluoromethoxy) phenylhydrazone (FCCP) and 1 µM rotenone plus 1 µM antimycin A were programmed. Calculations were performed following the manufacturer's instructions.

Whole Genome Bisulfite Sequencing (WGBS) analysis

5mC levels and genomic location was determined using whole genome bisulfite sequencing on *Tet3* knockout and wild-type E18.5 entire small intestinal epithelium. Two lines of each genotype were analyzed. Briefly, genomic DNA spiked with lambda DNA was fragmented to 200–400 bp. The DNA fragments were bisulfite treated using EZ DNA Methylation Gold kit (Zymo Research) to generate single strand DNA. Methylation sequencing adapters were ligated, followed by double strand DNA synthesis. Libraries were sequenced on an Illumina NovaSeq X Plus Series (PE150). Quality of the raw sequence reads was assessed with FastQC (fastqc_v0.11.8). Bismark software (version 0.24.0)[60] was used to perform alignments of bisulfite-treated reads to the reference genome. The reference genome was firstly transformed into a bisulfite-converted version and then indexed using bowtie2[61]. Sequence reads that produce a unique best alignment from the two alignment processes (original top and bottom strand) were then compared to the normal genomic sequence and the methylation state of all cytosine positions in the read was inferred. The same reads that aligned to the same regions of genome were regarded as duplicated ones. The sequences were divided into 10 kb bins to calculate their methylation level. The sum of methylated and unmethylated read counts in each window was calculated. Differentially methylated regions (DMRs) were identified using the DSS software[62]. According to the distribution of DMRs through the genome, genes were related to DMRs when their gene body region (from TSS to TES) or promoter region (upstream 2 kb from the TSS) have an overlap with the DMRs. Gene Ontology (GO) enrichment analysis of genes related to DMRs was implemented by the GOseq R package[63], in which gene length bias was corrected. GO terms with corrected *p*-value less than 0.05 were considered significantly enriched by DMR-related genes KOBAS software[64] was used to test the statistical enrichment of DMR-related genes in KEGG pathways. The WGBS and subsequent analysis were performed by Novogene. To identify putative enhancers on hypermethylated DMRs, H3K27ac and H3K4me1 ChIPseq data performed on murine intestinal cells at postnatal day 0 (P0) were downloaded from ENCODE (experiments: ENCSR642VYW and ENCSR159RVN) and used to identify enhancers in P0 intestinal cells (ENCFF660XDP.bed and ENCFF349IDR.bw for H3K27ac; ENCFF523POG.bed and ENCFF559NPS.bw for H3K4me1). Bedtools intersect was used to identify overlapping H3K27ac and H3K4me1 peaks with default parameters. Line plots and heatmaps were generated using deepTools.

MALDI-MSI measurement

All chemicals were purchased from Merck, if not otherwise mentioned. The first 2 cm of E18.5 mouse small intestines that include the whole duodenum and partial jejunum from wild-type and *Tet3* knockout embryos were dissected and fresh frozen in liquid nitrogen. Then, the samples were embedded in 7.5%HPMC-2.5%PVP[65] and cryo-sectioned for MALDI-MS imaging as described elsewhere[66]. Briefly, tissue sections were collected at 20 µm thickness and thaw mounted on Intellislides purchased from Bruker Daltonics. Slides were put in plastic mailers, vacuum sealed and stored at −80 °C until use. For MALDI MSI, a DAN-HCl matrix solution was prepared: 10 mg 1,5-diaminonaphtalene

(DAN), in 5 ml of solvent: 60% acetonitrile (ACN) in milliQ water (VWR) and 60 mM HCl. The matrix was sprayed using the HTX-M5 sprayer (HTX Technologies) with the following parameters: nozzle temperature 65 °C, passes 6, flow rate 0.07 ml/min, velocity 1200 mm/min, track spacing 2 mm, pattern CC, pressure 10 psi, drying time 10 s, and nozzle height 40 mm. After spraying, red phosphorus suspended in acetone was spotted on the slide for mass calibration purposes. MALDI MSI data was acquired on a timsTOF fleX system (Bruker Daltonics) at 5 μm in negative ion mode using 1,5-diaminonaphtalene (DAN) as matrix. MALDI MSI data was acquired on a tims-TOF fleX system (Bruker Daltonics) equipped with a smartbeam 3D 10 kHz laser and microGRID, controlled by TimsControl v4.1 and flexImaging v7.2 software (Bruker Daltonics). Data was acquired in negative ion mode, m/z range of 80–1300, with 25 laser shots per pixel, 10 kHz laser frequency, laser spot size 5 μm^2 and raster 5 μm. The tune parameters were the following: MALDI Plate Offset 50 V, Deflection 1 Delta −70 V, Funnel 1 RF 180 Vpp, isCID Energy 0 eV, Funnel 2 RF 180 Vpp, Multipole RF 180 Vpp, Collision Energy 3 eV, Collision RF 800 Vpp, Quadrupole Ion Energy 5 eV and Low Mass 70 m/z, Focus Pre TOF Transfer Time 80 μs and Pre Pulse Storage 6 μs, and Detection set to Focus Mode. After MALDI measurement, the matrix was removed by dipping the slide for 2 min in 100% methanol. An automated staining apparatus, SunTissuePrep (SunChrome) was used for hematoxylin and eosin staining. A coverslip was mounted on top using Eukitt as quick-hardening mounting medium. Data was imported into SCiLS Lab MVS, Version 2024b Pro, from Bruker Daltonics, using the standard import parameters. High resolution scan of the H&E stained slide was imported as ".svs" file using the *Import Optical Image* tool. The overview images and the high resolution scan were co-registered using three anchor points. For untargeted analysis, a first feature selection was done by setting an intensity threshold of 30.000 a.u. using the *Sliding Window* tool. A list of 2926 features was selected and used for bisecting *k*-means clustering in order to automatically separate the tissue area from the background area. A second feature list was generated using the *Find Discriminating Features (ROC)* tool with the threshold set to 0.65. A new list of 829 features was used for further analysis. Bisecting *k*-means segmentation using the new feature list, weak de-noising and correlation distance metric generated four regions of interest: red = muscle, yellow = base of the villi, green = center of the villi and purple/blue = tip of the villi. The villi were manually annotated based on the H&E staining scan and the segmentation image. The base and tip of four villi from each condition (WT and KO) were selected for statistical analysis. Annotation of features was done using HMDB database with 10 ppm mass error tolerance, adduct and isotope pattern matching through MetaboScape API inside SCiLS. All data was normalized by root-mean-square (RMS).

Cell culture

E18.5 tail tip–derived fibroblasts were cultured on gelatin using the following culture media: Knockout DMEM, 10% bovine fetal serum, 1X penicillin/streptomycin, 1X non-essential amino acids, 2 mM Glutamine and 0,1 mM β-Mercaptoethanol. *Atp5e* rescue experiments were performed on fibroblasts derived from E13.5 embryos and cultured as described above. *Tet3* knockout and wild-type fibroblasts were transduced with defective ecotropic retroviral particles coding for *Atp5e* or empty. The retroviral vector pMSCV-puro (Clontech) and the packaging pCL-Eco plasmid (Addgene #12371)[67] were used to generate the retroviral particles. After transduction, fibroblasts were selected with 1 μg/mL puromycin during 5 days. All experiments were performed using fibroblasts at passage 3.

Metabolomic analysis

Cells were fixed with 80% methanol, at 100 μL per 1 million cells. Cells were lysed with the aid of two metal balls at 30 Hz on a MM 400 mill mixer for 3 min, followed by centrifugal clarification at 21,000 g for 10 min. The clear supernatants were collected for the following assays. The precipitated pellets were used for protein assay using a standardized BCA procedure. For NAD and nucleotide quantification, an internal standard (IS) solution containing ^{13}C or ^{2}H-labeled NAD, NADH, AMP and ATP was prepared in 50% methanol. Serially diluted standard solutions of the targeted metabolites were prepared in 80% methanol. 10 μL of the clear supernatant of each sample or each standard solution was mixed with 40 μL of IS solution. 10 μL aliquots of the resultant solutions were injected into a C18 column to run UPLC-MRM/MS with (−) ion detection on a Waters Acquity UPLC system coupled to a Sciex QTRAP 6500 Plus MS instrument, using a tributylamine buffer solution and acetonitrile as the mobile phase for binary-solvent gradient elution. For GSH and GSSG quantification, an internal standard (IS) solution containing isotope-labeled GSH and GSSG was prepared in water. Serially diluted standard solutions of GSH and GSSG were prepared in 80% methanol. 20 μL of the clear supernatant of each sample or each standard solution was mixed with 80 μL of the IS solution. 10 μL aliquots of the resultant solutions were injected into a HILIC column to run UPLC-MRM/MS with (+) ion detection on an Agilent 1290 UHPLC system coupled to an Agilent 6495B QQQ MS instrument with the use of 0.1% formic acid in water and in acetonitrile as the mobile phase for binary-solvent gradient elution. For analysis of glucose, glucose-6P and mannose-6P, 50 μL of the supernatant of each sample was mixed with 50 μL of a solution of $^{13}C6$-glucose as internal standard, 100 μL of 25 mM AEC solution and 20 μL of acetic acid. The mixture was allowed to react at 60 °C for 70 min. After reaction, 300 μL of water and 300 μL of dichloroform was added. The mixture was vortex mixed and then centrifuged. The supernant was injected in 10-μL aliquots to run UPLC-MRM/MS with positive-ion detection on an Agilent 1290 UHPLC system coupled to a 4000 QTRAP mass spectrometer, as previously described[68]. The analysis of the TCA cycle carboxylic acids was carried out as previously described[69]. Briefly, 20 μL of the supernatant was mixed with 20 μL of a D- or 13-labeled analogue for each analyte as the internal standard, 20 μL of 200 mM 3-NPH solution and 20 μL of 150 EDC-6% pyridine solution. The mixture was allowed to react at 30 °C for 40 min. After reaction, the solution was diluted 3 fold with water. 20 μL was injected to run UPLC-MRM/MS with negative-ion detection on an Agilent 1290 UHPLC system coupled to a 4000 QTRAP mass spectrometer. Finally, quantification of other metabolites were performed as follows. 50 μL of each supernatant was mixed with 50 μL of water containing 50 pmol/mL GTP-13C10 and 50 μL of chloroform. The mixture was vortex mixed for 1 min, followed by centrifugation. 50 μL of each clear supernatant was taken out and mixed with an equal volume of water. 10 μL was injected to run UPLC-MRM/MS with negative-ion detection using a custom-developed reversed-phase LC-MRM/MS method for binary-solvent gradient elution. Concentrations of the detected analytes in the above assays were calculated with internal standard calibration by interpolating the constructed linear regression curves of individual compounds. The metabolomic analysis was performed in UVic Genome BC Proteomics Centre (Canada).

Statistical analysis

Data, unless otherwise stated, is represented as mean ± standard deviation. Two-tailed *t*-test was used to assess significant differences between groups.

Reporting summary

Further information on research design is available in the Nature Portfolio Reporting Summary linked to this article.

Data availability

The scRNA-seq and WGBS data generated in this study have been deposited in NCBI's Gene Expression Omnibus and are accessible through GEO Series accession number GSE171368 and GSE274671, respectively. Source data are provided with this paper.

References

1. Tan, L. & Shi, Y. G. Tet family proteins and 5-hydroxymethylcytosine in development and disease. *Development* **139**, 1895–1902 (2012).
2. Tahiliani, M. et al. Conversion of 5-methylcytosine to 5-hydroxymethylcytosine in mammalian DNA by MLL partner TET1. *Sci.* **324**, 930–935 (2009).
3. Uribe-Lewis, S. et al. 5-hydroxymethylcytosine and gene activity in mouse intestinal differentiation. *Sci. Rep.* **10**, 546 (2020).
4. Hahn, M. A. et al. Dynamics of 5-hydroxymethylcytosine and chromatin marks in mammalian neurogenesis. *Cell Rep.* **3**, 291–300 (2013).
5. Lio, C.-W. J. & Rao, A. TET enzymes and 5hmC in adaptive and innate immune systems. *Front. Immunol.* **10**, 210 (2019).
6. Dawlaty, M. M. et al. Tet1 is dispensable for maintaining pluripotency and its loss is compatible with embryonic and postnatal development. *Cell Stem Cell* **9**, 166–175 (2011).
7. Li, Z. et al. Deletion of Tet2 in mice leads to dysregulated hematopoietic stem cells and subsequent development of myeloid malignancies. *Blood* **118**, 4509–4518 (2011).
8. Dawlaty, M. M. et al. Combined deficiency of Tet1 and Tet2 causes epigenetic abnormalities but is compatible with postnatal development. *Dev. Cell* **24**, 310–323 (2013).
9. Gu, T.-P. et al. The role of Tet3 DNA dioxygenase in epigenetic reprogramming by oocytes. *Nature* **477**, 606–610 (2011).
10. Park, J. et al. Targeted erasure of DNA methylation by TET3 drives adipogenic reprogramming and differentiation. *Nat. Metab.* **4**, 918–931 (2022).
11. Fang, S. et al. Tet inactivation disrupts YY1 binding and long-range chromatin interactions during embryonic heart development. *Nat. Commun.* **10**, 4297 (2019).
12. Li, D. et al. Hepatic TET3 contributes to type-2 diabetes by inducing the HNF4α fetal isoform. *Nat. Commun.* **11**, 342 (2020).
13. Crosnier, C., Stamataki, D. & Lewis, J. Organizing cell renewal in the intestine: Stem cells, signals and combinatorial control. *Nat. Rev. Genet.* **7**, 349–359 (2006).
14. Yanai, H. et al. Intestinal stem cells contribute to the maturation of the neonatal small intestine and colon independently of digestive activity. *Sci. Rep.* **7**, 9891 (2017).
15. Maunoury, R. et al. Developmental regulation of villin gene expression in the epithelial cell lineages of mouse digestive and urogenital tracts. *Development* **115**, 717–728 (1992).
16. Haber, A. L. et al. A single-cell survey of the small intestinal epithelium. *Nature* **551**, 333–339 (2017).
17. Guerbette, T., Boudry, G. & Lan, A. Mitochondrial function in intestinal epithelium homeostasis and modulation in diet-induced obesity. *Mol. Metab.* **63**, 101546 (2022).
18. Rath, E., Moschetta, A. & Haller, D. Mitochondrial function — gatekeeper of intestinal epithelial cell homeostasis. *Nat. Rev. Gastroenterol. Hepatol.* **15**, 497–516 (2018).
19. Liesa, M. & Shirihai, O. S. Mitochondrial dynamics in the regulation of nutrient utilization and energy expenditure. *Cell Metab.* **17**, 491–506 (2013).
20. Gaffiero, P., Bergeron, M. & Thiery, G. Morphological study of cell organelles during development II-the mitochondria of the renal and intestinal epithelium. *Biol. Cell* **49**, 163–168 (1984).
21. Rodenburg, R. J. T. Biochemical diagnosis of mitochondrial disorders. *J. Inherit. Metab. Dis.* **34**, 283–292 (2011).
22. Babot, M., Birch, A., Labarbuta, P. & Galkin, A. Characterisation of the active/de-active transition of mitochondrial complex i. *Biochimica et. Biophysica Acta - Bioenerg.* **1837**, 1083–1092 (2014).
23. Kühlbrandt, W. Structure and Mechanisms of F-Type ATP Synthases. *Annu. Rev. Biochem.* **88**, 515–549 (2019).
24. Spikes, T. E., Montgomery, M. G. & Walker, J. E. Structure of the dimeric ATP synthase from bovine mitochondria. *Proc. Natl Acad. Sci. USA.* **117**, 23519–23526 (2020).
25. Ježek, P., Jabůrek, M., Holendová, B., Engstová, H. & Dlasková, A. Mitochondrial cristae morphology reflecting metabolism, superoxide formation, redox homeostasis, and pathology. *Antioxid. Redox Signal.* **39**, 635–683 (2023).
26. Mourier, A., Ruzzenente, B., Brandt, T., Kühlbrandt, W. & Larsson, N. G. Loss of LRPPRC causes ATP synthase deficiency. *Hum. Mol. Genet.* **23**, 2580–2592 (2014).
27. Perera, A. et al. TET3 is recruited by REST for context-specific hydroxymethylation and induction of gene expression. *Cell Rep.* **11**, 283–294 (2015).
28. Ketchum, H. C., Suzuki, M. & Dawlaty, M. Catalytic-dependent and -independent roles of TET3 in the regulation of specific genetic programs during neuroectoderm specification. *Commun. Biol.* **7**, 415 (2024).
29. Ansari, I. et al. TET2 and TET3 loss disrupts small intestine differentiation and homeostasis. *Nat. Commun.* **14**, 4005 (2023).
30. He, Y. et al. Spatiotemporal DNA methylome dynamics of the developing mouse fetus. *Nature* **583**, 752–759 (2020).
31. Schulz, S., Becker, M., Groseclose, M. R., Schadt, S. & Hopf, C. Advanced MALDI mass spectrometry imaging in pharmaceutical research and drug development. *Curr. Opin. Biotechnol.* **55**, 51–59 (2019).
32. Van Meer, G., Voelker, D. R. & Feigenson, G. W. Membrane lipids: where they are and how they behave. *Nat. Rev. Mol. Cell Biol.* **9**, 112–124 (2008).
33. Collard, F. et al. A conserved phosphatase destroys toxic glycolytic side products in mammals and yeast. *Nat. Chem. Biol.* **12**, 601–607 (2016).
34. Guimarães-Ferreira, L. Role of the phosphocreatine system on energetic homeostasis in skeletal and cardiac muscles. *Einstein (São Paulo, Braz.)* **12**, 126–131 (2014).
35. Folmes, C. D. L., Dzeja, P. P., Nelson, T. J. & Terzic, A. Metabolic plasticity in stem cell homeostasis and differentiation. *Cell Stem Cell* **11**, 596–606 (2012).
36. Gonzalez, E. A. et al. TET3-mediated DNA oxidation is essential for intestinal epithelial cell response to stressors. *Proc. Natl Acad. Sci. USA.* **120**, e2221405120 (2023).
37. Smillie, C. S. et al. Intra- and inter-cellular rewiring of the human colon during ulcerative colitis. *Cell* **178**, 714–730.e22 (2019).
38. Houštěk, J. et al. Mitochondrial diseases and genetic defects of ATP synthase. *Biochimica et. Biophysica Acta - Bioenerg.* **1757**, 1400–1405 (2006).
39. Čížková, A. et al. TMEM70 mutations cause isolated ATP synthase deficiency and neonatal mitochondrial encephalocardiomyopathy. *Nat. Genet.* **40**, 1288–1290 (2008).
40. Oláhová, M. et al. Biallelic mutations in ATP5F1D, which encodes a subunit of ATP synthase, cause a metabolic disorder. *Am. J. Hum. Genet.* **102**, 494–504 (2018).
41. Beck, D. B. et al. Delineation of a human mendelian disorder of the DNA demethylation machinery: TET3 deficiency. *Am. J. Hum. Genet.* **106**, 234–245 (2020).
42. Pfeifer, G. P., Xiong, W., Hahn, M. A. & Jin, S.-G. The role of 5-hydroxymethylcytosine in human cancer. *Cell Tissue Res* **356**, 631–641 (2014).
43. An, J. et al. Acute loss of TET function results in aggressive myeloid cancer in mice. *Nat. Commun.* **6**, 10071 (2015).
44. Tsiouplis, N. J., Bailey, D. W., Chiou, L. F., Wissink, F. J. & Tsagaratou, A. TET-Mediated Epigenetic Regulation in Immune Cell Development and Disease. *Front. Cell Dev. Biol.* **8**, 623948 (2021).
45. Tapia, N. et al. Reprogramming to pluripotency is an ancient trait of vertebrate Oct4 and Pou2 proteins. *Nat. Commun.* **3**, 1279 (2012).
46. Takashima, Y. et al. Resetting transcription factor control circuitry toward ground-state pluripotency in human. *Cell* **158**, 1254–1269 (2014).

47. Livak, K. J. & Schmittgen, T. D. Analysis of relative gene expression data using real-time quantitative PCR and the 2-ΔΔCT method. *Methods* **25**, 402–408 (2001).
48. Gracz, A. D., Puthoff, B. J. & Magness, S. T. Identification, isolation, and culture of intestinal epithelial stem cells from murine intestine. in *Somatic Stem Cells* 89–107 (2012).
49. Chen, J. et al. PBMC fixation and processing for Chromium single-cell RNA sequencing. *J. Transl. Med.* **16**, 198 (2018).
50. Srivastava, A., Malik, L., Smith, T., Sudbery, I. & Patro, R. Alevin efficiently estimates accurate gene abundances from dscRNA-seq data. *Genome Biol.* **20**, 65 (2019).
51. Wolf, F. A., Angerer, P. & Theis, F. J. SCANPY: large-scale single-cell gene expression data analysis. *Genome Biol.* **19**, 15 (2018).
52. Van Der Maaten, L. & Hinton, G. Visualizing data using t-SNE. *J. Mach. Learn. Res.* **9**, 2579–2625 (2008).
53. Jacomy, M., Venturini, T., Heymann, S. & Bastian, M. ForceAtlas2, a continuous graph layout algorithm for handy network visualization designed for the Gephi software. *PLoS One* **9**, e98679 (2014).
54. Raudvere, U. et al. G:Profiler: a web server for functional enrichment analysis and conversions of gene lists (2019 update). *Nucleic Acids Res* **47**, W191–W198 (2019).
55. Subramanian, A. et al. Gene set enrichment analysis: a knowledge-based approach for interpreting genome-wide expression profiles. *Proc. Natl Acad. Sci. USA.* **102**, 15545–15550 (2005).
56. Bayona-Bafaluy, M. P., Movilla, N., Pérez-Martos, A., Fernández-Silva, P. & Enriquez, J. A. Functional genetic analysis of the mammalian mitochondrial DNA encoded peptides: a mutagenesis approach. *Methods Mol. Biol.* **457**, 379–390 (2008).
57. Holgersen, E. M. et al. Transcriptome-wide off-target effects of steric-blocking oligonucleotides. *Nucleic Acid Ther.* **31**, 392–403 (2021).
58. Shepherd, D. & Garland, P. B. [2] Citrate synthase from rat liver. *Methods Enzymol.* **13**, 11–16 (1969).
59. Hernansanz-Agustín, P. et al. Na+ controls hypoxic signalling by the mitochondrial respiratory chain. *Nature* **586**, 287–291 (2020).
60. Krueger, F. & Andrews, S. R. Bismark: a flexible aligner and methylation caller for bisulfite-seq applications. *Bioinformatics* **27**, 1571–1572 (2011).
61. Langmead, B. & Salzberg, S. L. Fast gapped-read alignment with Bowtie 2. *Nat. Methods* **9**, 357–359 (2012).
62. Park, Y. & Wu, H. Differential methylation analysis for BS-seq data under general experimental design. *Bioinformatics* **32**, 1446–1453 (2016).
63. Young, M. D., Wakefield, M. J., Smyth, G. K. & Oshlack, A. Gene ontology analysis for RNA-seq: accounting for selection bias. *Genome Biol.* **11**, R14 (2010).
64. Mao, X., Cai, T., Olyarchuk, J. G. & Wei, L. Automated genome annotation and pathway identification using the KEGG Orthology (KO) as a controlled vocabulary. *Bioinformatics* **21**, 3787–3793 (2005).
65. Vande Voorde, J. et al. Metabolic profiling stratifies colorectal cancer and reveals adenosylhomocysteinase as a therapeutic target. *Nat. Metab.* **5**, 1303–1318 (2023).
66. Rittel, M. F. et al. Spatial omics imaging of fresh-frozen tissue and routine FFPE histopathology of a single cancer needle core biopsy: a freezing device and multimodal workflow. *Cancers (Basel).* **15**, 2676 (2023).
67. Naviaux, R. K., Costanzi, E., Haas, M. & Verma, I. M. The pCL vector system: rapid production of helper-free, high-titer, recombinant retroviruses. *J. Virol.* **70**, 5701–5705 (1996).
68. Han, J., Tschernutter, V., Yang, J., Eckle, T. & Borchers, C. H. Analysis of selected sugars and sugar phosphates in mouse heart tissue by reductive amination and liquid chromatography-electrospray ionization mass spectrometry. *Anal. Chem.* **85**, 5965–5973 (2013).
69. Han, J., Gagnon, S., Eckle, T. & Borchers, C. H. Metabolomic analysis of key central carbon metabolism carboxylic acids as their 3-nitrophenylhydrazones by UPLC/ESI-MS. *Electrophoresis* **34**, 2891–2900 (2013).

Acknowledgements

We are grateful to Dr. Sanz-Frasquet for ATP synthase structure annotation, A.Mota for the model illustration and Prof. Dr. A. Zorzano for discussion. N.T is funded by Agencia Estatal de Investigación (RYC-2014-16359; SAF2015-66549-R; PID2019-105920RB-100), Ayudas Fundación BBVA 2016 and Generalitat Valenciana (ACIF-2021-195). D.G. and M.J.A-B. have received funding from the European Union's Horizon 2020 Research and Innovation programme (grant agreement N° 899417), Ministerio de Ciencia e Innovación (PID2020-119715GB-I00/AEI/10.13039/501100011033) and Instituto de Salud Carlos III (Infrastructure of Precision Medicine associated with Science and Technology (IMPaCT) of the Strategic Action in Health (iDATA-MP)). J.P.B. is funded by MICIU/AEI (PID2022-138813OB-I00, PID2019-105699RB-I00 /10.13039/501100011033 and FEDER, UE), la Caixa Foundation (grant agreement LCF/PR/HR23/52430016) and the European Union's Horizon Europe research and innovation program under the MSCA Doctoral Networks 2021 (101072759; FuEl ThEbRaiN In healtThY aging and age-related diseases, ETERNITY).

Author contributions

I.M. and M.C-C. managed the animal colony and performed the immunostaining as well as qPCR experiments; C.G-C., M.C-C., and N.T. performed the electron microscopy experiments; D.G. and M-J.A-B. analyzed the single-cell RNA-seq data; G.W. and N.T. generated the knockout mouse model; S-A. I. performed the spatial metabolomics under the supervision of C.H., D. J-B., and I.M-R. analyzed and interpreted the mitochondrial membrane potential under J-P.B. supervision; C.G-C, A.C., and P.H-A. performed and interpreted the mitochondrial activity and assembly experiments under the supervision of J-A.E.; F-T. W. designed probes for mouse genotyping; H.K. analyzed enhancer enrichment under M-M.D. supervision; N.T. designed the project, performed the methylation analysis and other experiments, interpreted the experiments, provided financial support, and wrote the manuscript.

Competing interests

The authors declare no competing interests.

Additional information

Supplementary information The online version contains supplementary material available at https://doi.org/10.1038/s41467-024-54044-0.

Correspondence and requests for materials should be addressed to Natalia Tapia.

Peer review information *Nature Communications* thanks Patrick Varga-Weisz, and the other, anonymous, reviewer(s) for their contribution to the peer review of this work. A peer review file is available.

Reprints and permissions information is available at http://www.nature.com/reprints